Optical Properties of Graphene in the Terahertz Region

Samantha Scarfe

A thesis submitted in partial fulfillment
of the requirements for the degree of

MASTER OF SCIENCE
in Physics

Department of Physics
Faculty of Science
University of Ottawa

Abstract

This thesis explores the substrate-dependent charge carrier dynamics of large area graphene films. Using terahertz spectroscopy, we measure conductivity spectra of graphene supported by seven distinct substrates, and extract their transport properties (carrier scattering time, doping density, and carrier mobility) within the Drude model. We find that graphene supported by distinct substrates exhibit significantly different transport properties. We propose that graphene films supported by substrates with *less charged impurities* exhibit longer scattering times, and enhanced carrier mobilities, emphasizing the importance of the graphene-substrate interaction for optimization of device performance. These results will be significant for the effective integration of graphene into future technologies where an optimal carrier mobility is desired.

Acknowledgments

I would first like to extend the sincerest of thanks to my two co-supervisors, Professor Adina Luican-Mayer and Professor Jean-Michel Ménard. Their passion for science and care for crafting a well rounded student was evident throughout my degree. I feel they embody the best of what it means to co-supervise and am so grateful to have benefited from two times the mentorship.

I would also like to thank the students and post-docs I've had the pleasure to work with. Drs. Alexei Halpin and Lauren Gingras were true unicorn post docs, offering fountains of endless knowledge & support through key developments of this work. I'd also like to specially thank Wei Cui for his generous technical support in the THz lab, and Nick Couture for being both a fun and scientifically useful office mate. Thank you to Justin Boddison-Chouinard, and Ryan Plumadore for giving me a jump start in the world of 2D-materials fabrication, and for welcoming me into their clique.

Thank you to Tony Olivieri and Howard Northfield of the CRPuO cleanroom facilities for their patient training on many instruments, and for always offering the best advice or tricks for the tools.

Finally, my deepest of thanks goes to my family and friends. Specifically to my parents who have always supported my endeavors, and my fiance Nick who kept me sane at the end of many long days in the lab.

August 2020

Contents

List of Figures

List of Tables

Chapter 1

Introduction

1.1 Integrating two-dimensional materials for next-generation electronics

Layered (or van der Waals) materials are classified as those that have strong in plane covalent bonds and weak interlayer (van der Waals) bonds.[1] Due to this unique bonding structure, van der Waals materials have offered numerous advantages within materials-based applications, for example graphite and MoS_2 are widely used as dry lubricants.[2] Furthermore, individual layers can be straight forwardly isolated by breaking the weak van der Waals bonds, resulting in a new class of crystals known as *two-dimensional materials*. They refer to a class of crystals that are atomically thin, their electrons free to move in the two-dimensional plane, but restricted in their 3D motion by quantum mechanics.[3] The first truly two dimensional physical system was isolated[4] in 2004, when monolayer graphene was removed from bulk graphite. The first physical theory of the structure or behaviour of the material however dates to 1947, when Wallace considered the band behaviour of the compositional layers forming bulk graphite.[5]

Perhaps unsurprisingly, two-dimensional materials can exhibit many exceptional properties unique from those in 3D due to the reduced availability of phase space, and the reduction of bulk dielectric screening by neighboring layers.[6] For example, graphene exhibits linear dispersion and has massless-like carriers[1] (described in more detailed in

Section 1.2). Also notable, is the indirect bandgap in MoS_2 which becomes a *direct* gap in the monolayer, resulting in more efficient radiative recombination. Furthermore, the ability to custom construct materials based on selectable 2D-layer constituents (known as van der Waals heterostructures) allows exploration of novel collective phenomena. For example, the realization of atomic scale Moire pattern when graphene is supported by hBN (hexagonal boron-nitride).

2D material properties are of interest as the electronics and communications technology sector seeks to improve device performances through novel solutions. Currently, the FET (field effect transistor) is the backbone of silicon semiconductor electronics,[7] and consistent device progress depends on continued improvement in efficiency, namely through dimensional down-scaling of the FET[8] size. On the other hand, as the gate length is shortened in an FET, the channel thickness must also become thinner. In traditional semiconducting materials the carrier mobility degrades at thicknesses below 3 nm, presenting a limit to effective down-scaling. As physical limits to the FET size are reached, materials that can provide smaller gate lengths with maintained high carrier mobility will be in demand.

2D materials suitable for supporting FET technology are those with a bandgap, to allow for on/off logic switching. This includes MoS_2, WS_2, or black phosphorus (BP), as 2D semiconductors typically have larger mobile carrier densities and thus can carry higher current. Furthermore, the atomic scale thickness allows for excellent electrostatic gating control, and the gate channel lengths can be made smaller.[1] In fact, using a carbon nanotube as the gate electrode, an MoS_2 based FET was fabricated with gate length of just 1 nm.[9] Due to graphene's atomic thickness and high mobility, there was at first much optimism that it would contribute to improved FET performance, until the incompatibility due to a lack of bandgap became evident.

Still yet, there are many opportunities for graphene to contribute to next-gen electronics that aren't 'computational' logic based systems, called *more than Moore* technologies. These can range from systems such as photodetectors and modulators for image sensors, to data communications, to flexible gas/chemical sensing. This thesis is centered on the study of graphene, and the remainder of this section motivates how it can be incorporated into technologies that exploit its unique properties, keeping in mind the limitations imposed by the zero-gap band nature.

Graphene detectors and modulators offer the benefits of high speed, wide spectral bandwidth (due to the lack of bandgap), low power consumption and straight forward integration into Si-CMOS circuitry (which represent the heart of imaging systems).[8] Furthermore, due to the high mobility it offers ultrafast conversion of photons to current.[10] A broadband image sensor array based on graphene-CMOS integration was reported[11] that was able to operate as a digital camera between 300 - 2000 nm. CVD graphene is directly transferred onto the Si-CMOS chip and is patterned to form channels connecting pixels. PbS quantum dots (QDs) are spun on top of the graphene. The photoresponse is based on photoexcited QDs injecting holes to the graphene channel which then traverse the biased channel with high mobility (~ 1000 cm^{2}V^{-1}s^{-1}) resulting in better gain and responsivity as compared to devices without graphene.[12]

Graphene has also found promise within the chemical, gas, and biosensing community. Due to its high surface to volume ratio, it is highly sensitive to adsorbed molecular species,[13] and has demonstrated suitable response for efficient sensing of many gases such as (but not limited to) NH_3, ethanol, H_2, CO, O_2.[14–16] Sensing measurements are typically performed in a chemiresistor geometry, where the resistance of a graphene sheet is monitored during exposure to a gas. As a molecular species adsorbs to the graphene film, they either act as an electron acceptor or donor, and subsequently increase or decrease the measured resistance. Flexible and wearable graphene based sensors are currently an evolving field, as bendable electronics become increasingly attractive to applications in healthcare, prosthetics, robotics, aerospace, military, and more.[17] Recently, a flexible graphene based radio frequency antennae sensor was demonstrated, that maintained integrity under controlled compression and tensile bending.[18] It operates between 3.13 and 4.42 GHz, and represents an application for graphene that will be particularly of use throughout the development of the Internet of Things, and the popularity of wearable electronics.

Graphene integrated electronics are typically interested in exploiting a high carrier mobility. Importantly, the mobility in graphene is understood to be sensitive to it's environment, often dominated by the supporting substrate. Therefore, how the substrate influences mobility is important for integration. Several well understood techniques for characterizing the transport properties, including mobility of graphene, exist and are described within this thesis. They range in invasiveness and need for physical contact. It has been established that spectroscopy of graphene films in the low energy terahertz (THz) region is a suitable way of probing graphene mobility.[19–22] Conveniently, this technique does not physically alter the graphene, leaving it usable after characterization. It also can be performed on many substrates, so long as they are sufficiently THz transparent. This opens the door for minimally invasive and efficient mobility extraction of graphene supported by diverse environments and substrates. This thesis addresses the role substrate plays in limiting the mobility, using the non-contact technique of THz spectroscopy. The results presented herein will be important to the body of knowledge surrounding substrate dependent carrier dynamics as there is an increasing desire to integrate graphene into next-generation technologies.

1.2 Graphene and its electronic properties

Many of graphene's remarkable transport properties originate from its band structure, a consequence of the simple hexagonal crystal lattice as discussed below.

Lattice & band structure

Graphene is composed of carbon atoms arranged in a hexagonal lattice as shown in Figure 1.1. Carbon atoms hybridize with one another in plane, each forming three sp^2 orbitals. Overlapping sp^2 orbitals of neighboring carbon atoms hybridize to form strong covalent bonds with their nearest neighbour. This arrangement leaves one p orbital de-localized in the perpendicular plane.

The resulting honeycomb lattice can be represented as a triangular lattice with a basis of two atoms per unit cell (an A and B atom). The lattice vectors in this picture are written as:

$$\vec{a_1} = a_0(\frac{\sqrt{3}}{2}\hat{x} + \frac{3}{2}\hat{y}) \quad \vec{a_2} = a_0(\frac{\sqrt{3}}{2}\hat{x} - \frac{3}{2}\hat{y}), \tag{1.1}$$

where $a_0 = 1.42$ $\mathring{A}$ is the distance between nearest neighbour carbon atoms. The reciprocal lattice vectors are then calculated as:[23]

$$\vec{b_1} = \frac{2\pi}{a_0}(\frac{1}{\sqrt{3}}\hat{x} + \frac{1}{3}\hat{y}) \quad \vec{b_2} = \frac{2\pi}{a_0}(\frac{1}{\sqrt{3}}\hat{x} - \frac{1}{3}\hat{y}) \tag{1.2}$$

The reciprocal lattice space for graphene is also a honeycomb structure, with a 90° rotation relative to the real space. The first Brillouin zone is a hexagon, spanned by $\vec{b_1}$ and $\vec{b_2}$. At the corners of the first Brillouin zone are the K and K' points that form two independent sublattices within reciprocal space where K = $\left(\frac{4\pi}{3\sqrt{3}a_0}, 0\right)$ and K' = $\left(\frac{2\pi}{3\sqrt{3}a_0}, \frac{2\pi}{3a_0}\right)$. The low energy electronic behaviour of carriers in graphene is governed by the resulting band structure around these points, as discussed later.

The electronic band structure of graphene was first calculated by Wallace[5] in 1947 when he considered the layers of bulk graphite as independent planes. Here, we consider only nearest neighbour interactions of the delocalized p electrons (those between vectors $\delta_{1,2,3}$, or hopping between A and B sites).[24] For a given sublattice in real space, the three

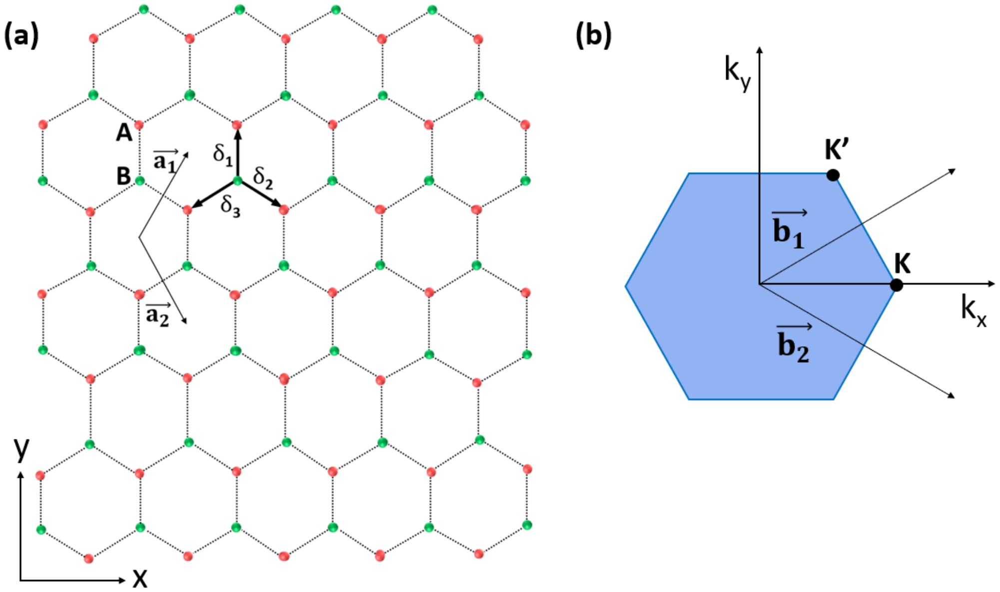

Figure 1.1: (a) The honeycomb lattice structure of graphene, highlighting the carbon atoms on the A sublattice in red and the B sublattice in green. Lattice vectors are $\vec{a_1}$ and $\vec{a_2}$. Nearest neighbour atoms are indicated δ_i, i = 1,2,3. (b) First Brillouin zone, with reciprocal lattice vectors $\vec{b_1}$ and $\vec{b_2}$. The valence and conduction bands at the K and K' points.

nearest neighbour vectors are written as:

$$\vec{\delta_1} = a_0(\hat{y}), \quad \vec{\delta_2} = a_0(\frac{\sqrt{3}}{2}\hat{x}, -\frac{\hat{y}}{2}), \quad \vec{\delta_3} = a_0(-\frac{\sqrt{3}}{2}\hat{x}, -\frac{\hat{y}}{2}) \tag{1.3}$$

The tight binding Hamiltonian is then given by[25] $H_{ij} = \langle \Psi_i | \hat{H} | \Psi_j \rangle$ where i and j index hopping between the A and B sublattices and $\Psi_{i,j}$ represent the eigenstates for the two atomic sites. This Hamiltonian takes into account all possible p orbital hybridizations between atoms on the two sublattices. The Hamiltonian can be written in matrix form as

$$H = \begin{pmatrix} H_{AA} & H_{AB} \\ H_{BA} & H_{BB} \end{pmatrix} = -t \begin{pmatrix} 0 & f(\vec{k}) \\ f^*(\vec{k}) & 0 \end{pmatrix}, \tag{1.4}$$

where $t \approx 2.8$ eV is the nearest neighbour hopping parameter, and $f(\vec{k})$ is defined for the three nearest neighbour interactions to be

$$f(\vec{k}) = \sum_{n=1}^{3} e^{i\vec{k}\vec{\delta}_n} = e^{\frac{ik_y a}{\sqrt{3}}} + e^{\frac{ik_x a}{2}} e^{\frac{-ik_y a}{2\sqrt{3}}} + e^{\frac{-ik_x a}{2}} e^{\frac{-ik_y a}{2\sqrt{3}}}, \tag{1.5}$$

where $a = \sqrt{3}a_0 = 2.46\ \mathring{A}$ is the length of the unit cell vectors. This function sums over all the nearest neighbour atoms. We can simplify $f(\vec{k})$ as

$$f(\vec{k}) = e^{\frac{ik_y a}{\sqrt{3}}} + 2e^{\frac{-ik_y a}{2\sqrt{3}}} \cos(\frac{k_x a}{2}) \tag{1.6}$$

To find the eigenvalues of this tight binding Hamiltonian we have to solve the Schrodinger equation $\hat{H}\Psi = E\Psi$ with:

$$det|H - E| = \begin{pmatrix} -\epsilon & tf(\vec{k}) \\ tf^*(\vec{k}) & -\epsilon \end{pmatrix} = 0 \tag{1.7}$$

$$\epsilon^2 - t^2\sqrt{f^*(\vec{k})f(\vec{k})} = 0 \tag{1.8}$$

$$\epsilon_\pm(\vec{k}) = \pm t|f(\vec{k})| \tag{1.9}$$

The energy bands corresponding to this tight binding Hamiltonian are then calculated to be:

$$\epsilon(\vec{k}) = \pm t\sqrt{1 + 4\cos\left(\frac{ak_x}{2}\right)\cos\left(\frac{\sqrt{3}ak_y}{2}\right) + 4\cos^2\left(\frac{ak_x}{2}\right)} \tag{1.10}$$

In the resulting band structure as shown in Figure 1.2a, the conduction (valence) band is represented as the positive (negative) term. The bands meet at the six corners of the Brillouin zone (BZ), which is outlined in red in Figure 1.2a. These corners form

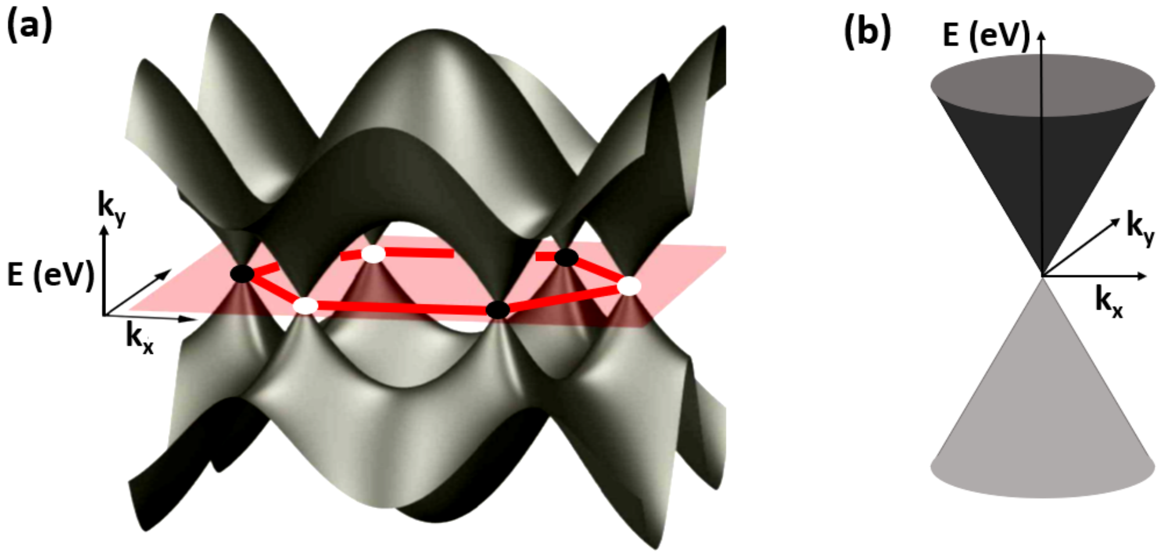

Figure 1.2: (a) Band structure for graphene calculated using the tight binding Hamiltonian. Taken from[27] (b) Zoom in of the band structure near the Dirac points, highlighting the conical dispersion near $\epsilon = 0$ eV.

three pairs of non-degenerate K and K' points, also called the Dirac points. They are pictured as white and black dots along the BZ corners. There is no overlap of the conduction and valence band at the Dirac points, making graphene a gapless semi-conductor. Furthermore, the band behaviour is symmetric for electron and hole bands. Finally important to mention, is the two-component wave function of graphene is described in terms of a "pseudospin"vector arising from the existence of two sublattices.In graphene the pseudospin vector is locked parallel or antiparallel to the momentum vector and is conserved through scattering events, limiting the scattering mechanisms possible to those that don't involve complete backscattering.[26]

In neutral graphene each carbon atom has one out of plane electron, and the Fermi level sits at $\epsilon = 0$, at the six corners of the BZ (the K points). Therefore, in neutral graphene, the Fermi surface is composed of the six Dirac points, there is no net doping of electron or hole carriers, and graphene conduction exhibits maximum resistance.

Linear dispersion

If we expand the Hamiltonian calculated in Equation (1.10) near the K point by considering the relative momentum to be $\mathbf{q} = \mathbf{k} - \mathbf{K}$, we write $f(\vec{k})$ in terms of $\mathbf{q}$ as

$$f(\vec{k}) = f(\mathbf{q}+\mathbf{K}) = e^{\frac{iq_y a}{\sqrt{3}}} + 2e^{\frac{-iq_y a}{2\sqrt{3}}} \cos\left(\frac{a(q_x + \frac{4\pi}{3a})}{2}\right) \tag{1.11}$$

Taylor expansion about $\mathbf{q} = 0$ to first order, gives

$$f(\vec{k}) \approx -a\frac{\sqrt{3}}{2}(q_x - iq_y) \tag{1.12}$$

And for the energy band structure near this point

$$\epsilon_\pm = \pm t|f(\vec{k})| \approx \pm ta\frac{\sqrt{3}}{2}|\mathbf{q}| \tag{1.13}$$

implying that the energy dispersion is linear in momentum near the K point. This is illustrated in Fig 1.2b, where we can see the conical shape of the dispersion at low energy, near K and K' points. Importantly, the Fermi level of graphene is almost always situated within the linear dispersion regime, allowing complications from large q to be neglected.[28] Finally, the electron velocity near these points is known as the Fermi velocity (v_F) where $v_F = \frac{1}{\hbar}|\frac{d\epsilon}{dq}| = \frac{ta}{\hbar}\frac{\sqrt{3}}{2}$ and is equal to 1.1×10^6 m/s. This results in:

$$\epsilon_\pm(\mathbf{q}) \approx \pm v_F|\mathbf{q}| \tag{1.14}$$

In traditional materials with parabolic band dispersion, $\epsilon = \frac{(\hbar k)^2}{2m}$, and subsequently $v = \frac{\hbar k}{m} = \sqrt{\frac{2\epsilon}{m}}$, and hence the carrier velocity changes substantially depending on the energy or momentum. In graphene, which has a conical dispersion, the carrier velocity is independent of energy and of momentum. This implies that carrier movement is analogous to the relativistic motion of particles with zero rest-mass, described by the Dirac equation.[28]

Owing to this unusual linear band structure and resulting quasi-relativistic carrier behaviour, graphene has opened the door for new fundamental physics experiments, and offered hope for functional applications. From the former's perspective, graphene has provided means for studying 'quantum relativistic' phenomena in table-top experiments.[29] As mentioned, the Fermi velocity of carriers in such a band structure is 1.1 $\times 10^6$ m/s, 1/300 the speed of light. This gives charge carriers an effective 'speed of light'[30] as they move in the honeycomb periodic potential. Fundamental science experiments made possible include investigation of the Klein paradox,[31] and the quantum hall effect.[32] Graphene also exhibits a strong ambipolar field effect, meaning charge carrier type can be continuously tuned between holes and electrons in high concentrations ($\sim 10^{13}$ cm^{-2}). It demonstrates extraordinarily high mobilities[33] (as high as 10^6 $\text{cm}^2\text{V}^{-1}\text{s}^{-1}$ at low temperature[34]), and room temperature ballistic transport across micrometer distances.[35] These properties make graphene an attractive candidate for implementation into transport applications in both photonic and electronic devices.

1.3 Overview

As mentioned, this thesis will outline the implementation of THz spectroscopy to probe the transport dynamics of large area graphene films supported by several distinct substrates. It aims to investigate how the substrate plays a role in limiting the transport performance. It will be structured in the following manner:

Chapter 2 will provide background on the fabrication techniques for preparing micron-scale and centimeter-scale graphene samples. It will also cover several metrological characterization techniques implemented to optimize and standardize the fabrication procedure. Finally, it will introduce the interaction and resulting conductivity relation of graphene carriers with infrared light, specifically with terahertz photons.

Chapter 3 is an introduction to the principles of time domain terahertz spectroscopy. It presents an introductory theory to the nonlinear optical processes used to generate, and to detect THz frequencies. It walks through the experimental apparatus employed in our lab's spectrometer, and the theoretical analysis that is standard for extracting the conductivity of thin conducting graphene films from transmission spectroscopy.

Chapter 4 discusses in more detail how to extend the extracted conductivity spectra to calculating specific transport properties of large area graphene films. This includes the DC conductivity (σ_{DC}), the average scattering time (τ), the extrinsic carrier doping density (N_s), and the carrier mobility (μ). It discusses how graphene supported by distinct substrates can exhibit vastly different carrier properties, and aims to explain how this can be understood through the substrates density of charged impurities.

Chapter 2

Experimental techniques: Sample preparation

2.1 Fabricating graphene samples

Graphene made the leap from a theoretical model to an experimental system with Geim and Novoselov's 2004 work that studied graphene based FETs.[4] In this work, graphene samples were isolated for the first time by peeling back layers from bulk graphite crystals with adhesive tape. The procedure is called mechanical exfoliation, and is now a standard technique in two-dimensional materials laboratories. While this top down approach produces graphene flakes of high crystalline quality and with minimal defects, it is arduous (the user has to search for regions of monolayer under a microscope), and samples are typically limited in size to $\sim$100 μm^2.

With the motivation for pursuing scalable applications where graphene can be implemented in industry, there are now many growth and preparation techniques for fabricating large scale films from the atomic precursors. Bottom up approaches in use today include epitaxial growth on SiC substrates,[36] and chemical growth by catalyzed chemical vapor deposition.[37] In this section, I will review the experimental process to fabricate graphene samples used within this work.

2.1.1 Transfer techniques

Mechanical exfoliation

As mentioned, the first graphene samples were prepared with a technique called mechanical exfoliation.[4,30] The technique is remarkably simple. Starting from a bulk crystal of highly oriented pyrolitic graphite (HOPG) we apply adhesive tape and peel back. This piece of tape is then attached to a second piece, and the peel back is repeated, further thinning down the initially isolated HOPG. As this process is iterated, the normal force from the tape overcomes the van der Waals force between adjacent graphene layers, and thinner layers of the HOPG crystal are isolated, eventually leaving graphene. Finally, the tape is pressed onto and peeled off of an Si-SiO_2 substrate, leaving exfoliated graphite crystal of many different thicknesses behind. For very specific SiO_2 thicknesses (either 90 nm or 280 nm) graphene films demonstrate suitable optical contrast, and become visible to the eye with white light illumination under a microscope.[38] We can place the sample under the optical microscope in reflected bright field mode, and search for films that are likely monolayer based on their visual contrast and color. Monolayer flakes appear a light purple, few layer flakes are brighter blue, and thick graphite is green, yellow, or grey depending on the exact thickness.[38]

New techniques have been developed for creating novel materials based on selectively chosen constituent layers fabricated by mechanical exfoliation. Using this technique, layers can be selected for desired thickness based on the optical contrast, lifted off the substrate, and transferred to other two-dimensional materials to make hybrid heterostructures not found in nature.[39] Examples of this method are presented below in Figure 2.1, with graphene stacked on rhenium disulfide and hexagonal boron-nitride respectively.

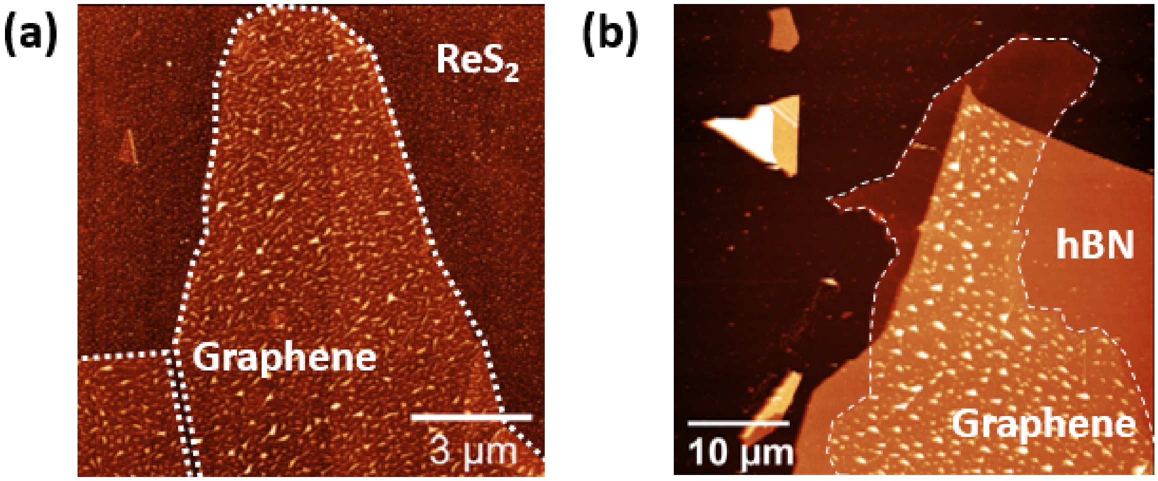

Figure 2.1: Mechanically exfoliated graphene (indicated by the white dashed line) supported by (a) rhenium disulfide and (b) hexagonal boron nitride.

Chemical vapor deposition

Since 2009, the bottom up approach of synthesizing monolayer graphene based on chemical vapor deposition (CVD) has proven to be a promising solution in fabricating large area, scalable films[37].[40] Today, sheets of monolayer graphene can be fabricated by CVD with dimensions as large as 30 inches in the diagonal direction.[41] CVD graphene is made by flowing hydrogen and methane gas through a furnace heated to temperatures up to 1000°C using selected metallic foil as a catalyst in the growth chamber.[37] Through delicate control of the chamber pressure, temperature, and gas composition, the methane decomposes and allows for carbon atoms to settle on the metallic foil, forming graphene. In this work, we use commercially purchased CVD graphene (Graphenea) on (4x3 inch) copper foils.

The first required step in using the CVD graphene is to transfer it from the copper foil, to a desired substrate. The challenge is to apply a transfer technique that (i) results in minimal surface modifications, (ii) leaves minimal residue, and (iii) preserves the electrical properties of the graphene. This challenge of cleanly transferring large area

CVD graphene has been addressed by several groups,[42–45] each unique in their transfer chemistry or in the overall physical method. The most common transfer process involves wet etching of the copper foil and directly picking up the graphene from below with the substrate[46].[47]

To begin, we cut the graphene-copper foil into (1×1 cm) samples using thread scissors rinsed with isopropyl alcohol (IPA) (Figure 2.2a). The next step is to spin coat a layer of resist on the samples, that will act as a stabilizing backbone during the wet etch.

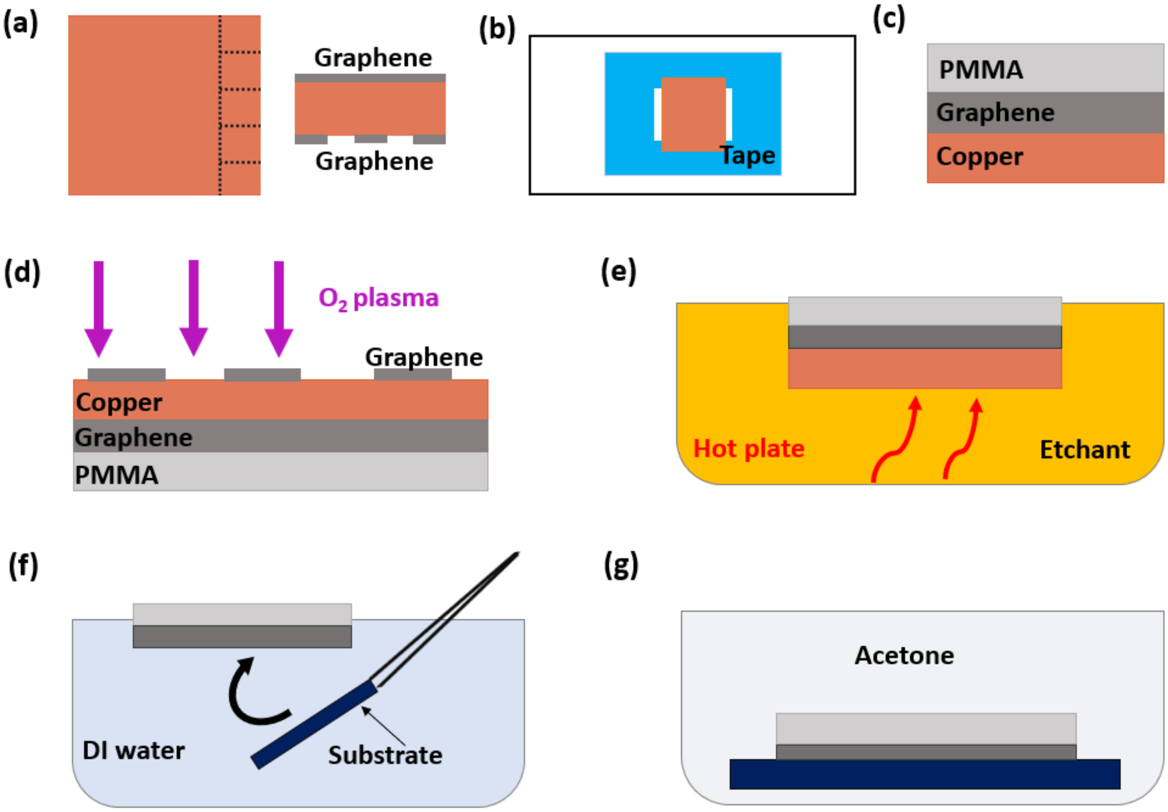

Figure 2.2: Steps of the CVD graphene transfer procedure. (a) Schematic of copper foil covered in graphene. Dashed lines represent the geometry of cutting to prepare individual samples. (b) Sample mounted to a glass slide with adhesive tape to deposit and spin-coat PMMA. (c) Sample as prepared after PMMA supporting layer is spun. (d) Sample backside is exposed to oxygen plasma to remove the graphene layer. (e) Sample is placed in copper etchant. (f) Sample is transferred to a water bath to rinse and pick up. (g) Sample is placed in acetone to dissolve the PMMA layer.

Since the copper foils are so thin, they require a stable support to be mounted on the spinner. To provide this, we tape the sample on a glass slide (Figure 2.2b), secure the slide and sample on the spinner, and pipette a small drop of the PMMA resist on the copper square. We begin spinning immediately, applying 3000 RPM for 60 seconds, resulting in a PMMA layer about 200 nm thick (Figure 2.2c).

Importantly, during the CVD process graphene grows on both sides of the copper foil. Graphenea partially removes the backside graphene, however not completely (this is visualized in the right panel of Figure 2.2a). If it is not removed it can remain beneath the surface, trap molecules of copper foil, and diminish the quality of the final transferred CVD film.[48] To remove it we place samples upside down in a reactive ion etcher (RIE) and expose them to 10 sccm of O_2 plasma at 100 W for 1 minute at 1.1 Pa (Figure 2.2d). The RIE applies plasma from the top down, and with the desired graphene film protected by a layer of PMMA, it is preserved throughout the etch and not damaged.

Next, we place the sample in a dish of commercially mixed copper etchant (Sigma Aldrich) on a hot place set to 70°C (Figure 2.2e). The elevated temperature increases the etching rate, allowing this step to take between only 10-60 minutes. The etch is considered complete when there is visually no copper remaining. The transparent graphene-PMMA film is then lifted out using an etchant resistant spoon and placed into a dish of distilled water for 5 minutes. This is repeated for two more distilled water dishes, each providing an increasingly clean rinse of the copper etchant. After the last water rinse is complete, the desired substrate is introduced into the dish from below and delicately raised towards the graphene-PMMA film at a 45-degree angle (Figure 2.2f). The graphene-PMMA film is left in a sample holder inside a fumehood environment for eight hours to allow any water that may have been captured between the sample and substrate to evaporate, and to promote adhesion of the graphene film to the substrate. The PMMA film is dissolved the next day by placing the sample in a bath of warm acetone at 50°C for 1 hour (Figure 2.2g). The final result is a (1×1 cm) CVD graphene layer supported by the substrate it was picked up with.

We note that for the purpose of performing THz spectroscopy, we delicately place the sample so that it covers half of the substrate as show in Figure 2.3. This allows transmission measurements on and off of the graphene without changing the sample in the optical setup. Substrates that were selected for this study aim to reflect those that could likely be used in applied graphene-integrated future technologies, and are briefly introduced below.

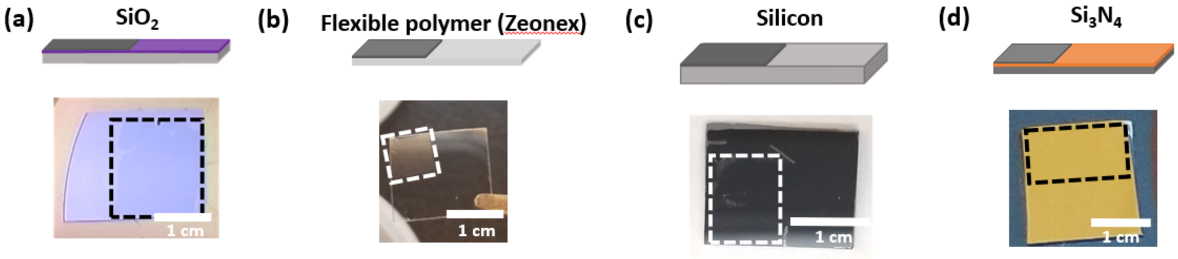

Figure 2.3: CVD graphene transfers onto several substrates. (a) Si-SiO_2 wafers. (b) Transparent and flexible polymers (c) Silicon wafers without a grown oxide. (d) Si-Si_3N_4 wafers.

Doped silicon

Graphene has been considered appealing for integration into a variety of silicon photonic applications,[49] ranging from compact and low loss phase modulators[50,51] to improved photodetection schemes.[10,52] It is therefore important to understand the transport limitations of graphene carriers on silicon wafers. For this reason we choose to deposit graphene on silicon wafers with a controlled density of injected boron impurities. We compare the mobility performance of graphene deposited on high purity silicon (10,000 Ω-cm resistivity), to that of more heavily doped silicon (1-10 Ω-cm and 10-20 Ω-cm resistivity). Silicon with lower resistivity has an increased density of injected boron dopants, that will likely act as scattering potentials which limit the graphene carrier mobility. The impurity concentration based on the reported resistivity for the three substrates are written in Table 2.1.

Silicon resistivity	**10,000 Ω-cm**	**15 Ω-cm**	**5 Ω-cm**
Impurity conc.[53]	1.326×10^{12} cm^{-3}	9.001×10^{14} cm^{-3}	2.762×10^{15} cm^{-3}
Avg. dopant spacing	0.911 μm	0.104 μm	0.0713 μm

Table 2.1: The resistivity of three silicon substrates used within this work, and their manufacturer reported boron doping density in terms of impurity concentration. We also calculate the average spacing between dopants, based on the assumption they are equally spaced.

Transparent & flexible polymer

Graphene is regarded for many of its physical properties including its strength and flexibility, particularly for applications within electronic devices that themselves are flexible or conformal.[54] Graphene based flexible FETs have been demonstrated with graphene on flexible substrates that both do[55] and do not[56,57] have a flexible gate dielectric. For this work, we deposit graphene on the flexible transparent substrate called ZEONEX®, a cyclo-olefin polymer. ZEONEX® is a strongly insulating material, with a reported resistivity of 10^{16} Ω-cm.[58]

Si-SiO$_2$

SiO$_2$ is currently the prevailing gate dielectric for silicon based metal oxide semiconductor devices.[59] Naturally, we have included this substrate within the study. SiO$_2$ is deposited on silicon under elevated temperatures (between 800 and 1300°C) by what is known as thermal growth. This technique can be classified into two groups, dry and wet thermal growth. In dry thermal growth, the silicon wafer is exposed to pure oxygen gas, and the SiO$_2$ grows slowly. In wet thermal growth the silicon wafer is exposed to water vapor, SiO$_2$ then grows (at a faster rate compared to in dry growth), and hydrogen gas is released as a byproduct. Dry thermal SiO$_2$ is considered to be cleaner, since the slower growth process results in fewer dangling bonds at the silicon interface, and therefore a smaller amount of states for trapped charge to accumulate. For this work we study graphene deposited on both of these types of SiO_2.

Si_3N_4-silicon

Si_3N_4 has been used as a gate dielectric for GFET devices, due to its higher dielectric constant compared to SiO_2.[60] It is thought that a substrate with higher dielectric constant can be used to effectively screen charged impurities, and overall improve the device mobility.[61] In this work we deposit graphene on 300 nm thick Si_3N_4 dielectric films grown by chemical vapor deposition.

Making field effect transistors based on CVD graphene

CVD graphene has also been used to fabricate large area graphene field effect transistors. These can be used as sensors for sensitive detection of chemicals including water vapor, ethanol, and methanol.[14] Detection is done by monitoring the resistance of the graphene device over time as the sensor is exposed to a trace chemical. Devices are fabricated based on the above described transfer procedure, and placed on Si/SiO_2 wafers as a substrate. Devices are then mounted in a Thermo/Electron Beam Evaporator (Nexdep Series, Angstrom). A shadow mask is placed in front of each sensor during the deposition of two metallic electrodes (5 nm Ti/150 nm Au) as in Figure 2.4a. The shadow mask extends the length of the graphene film and onto the substrate, as metal adhesion to the underlying SiO_2 film is superior to metal adhesion to graphene. The sample is removed from the evaporator and mounted onto an electronic board where it can be wire bonded at a source and drain electrode to perform resistance measurements under exposure to chemical analytes (Figure 2.4b).

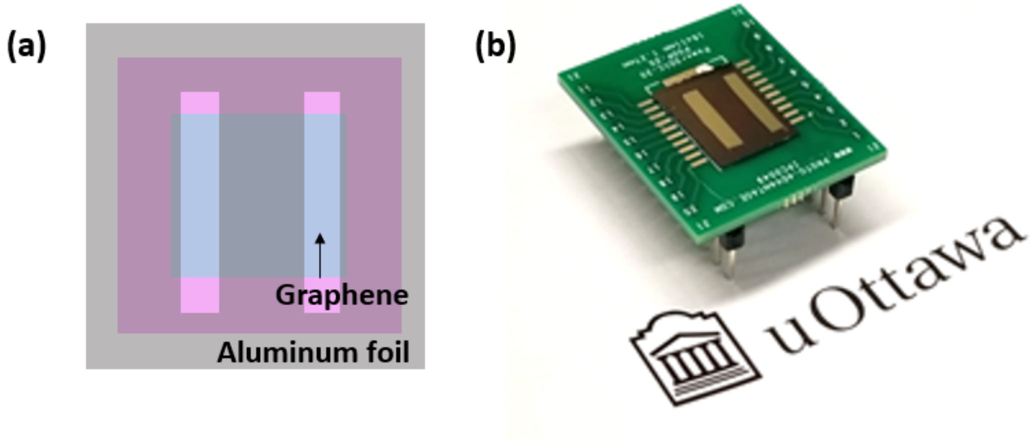

Figure 2.4: (a) Schematic of CVD graphene underneath an aluminum foil shadow mask, as would be mounted in the metal evaporator. The mask consists of two strips that extend the length of the graphene film and overlay onto the substrate to improve adhesion. (b) Graphene FET as mounted on a printed circuit board and configured to perform resistance measurements.

2.1.2 Optimizing the graphene surface

Graphene preparation methods typically involve the use of adhesives, or polymer supports that leave residues on the graphene surface or trapped at the graphene substrate interface. Residues can be polymer aggregates, trapped water molecules, or trapped hydrocarbons suspended in the ambient air during the transfer.[62] The following section will review cleaning methods applied to graphene samples within the context of this work.

Temperature annealing

Cleaning large area graphene films after they have undergone the wet transfer procedure is typically done using acetone as a solvent to dissolve the PMMA support layer. The sample is placed in a dish of warm acetone (50°C) for 1 hour. However, acetone cannot completely remove PMMA residues with 100% efficiency. This is evident in Figure 2.5a, which is an AFM micrograph of a CVD graphene surface after one hour in acetone. It has been demonstrated[63] that these contaminants can be removed from the graphene surface by placing the sample in a furnace under continuous flow of H_2/Ar gas. In samples presented here, PMMA coverage is considerably reduced from ~25% without annealing (Figure 2.5a), to ~8% (Figure 2.5b), to < 1% (Figure 2.5c) after annealing at 400°C for 1 and 9 hours respectively.

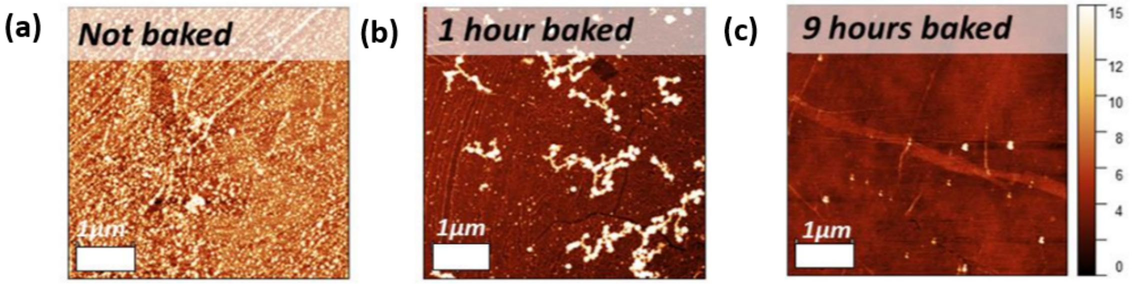

Figure 2.5: (a) AFM micrograph of a CVD graphene surface after rinsing the sample in acetone for 1 hour. (b) AFM micrograph of a CVD graphene surface after rinsing in acetone, and heating the sample to 400°C in H_2/Ar for 1 hour. (c) AFM micrograph of a CVD graphene surface after rinsing in acetone, and heating the sample to 400°C in H_2/Ar for 9 hours.

Cleaning exfoliated graphene flakes selectively

Thermal treatments as described above are an efficient and non-invasive method of removing residues from the graphene sample. However, the technique is non-targeted, and for certain graphene based devices there are specific regions where it may not be suitable to apply heat (such as at a metal contact). Within this work it was found that graphene surfaces can be selectively cleaned of transfer residues by applying targeted heating from a focused laser beam.[64] The method relies on the same physical principles as the general diffusive heat treatment presented above, the laser locally applying heat. However, this heat is applied in an intentional manner with the targeted and spatially resolved capabilities of a local probe.

This phenomena was observed by preparing graphene supported by different substrates, namely rhenium disulfide (ReS_2) and hexagonal boron nitride (hBN). These samples were prepared with mechanical exfoliation and subsequent stamping on the substrate, and resulted in flakes of graphene around 100 μm^2 in size. Residues typical of the stamping transfer are shown in the AFM micrograph shown in Figure 2.6a as aggregated blisters. They become even more evident in the zoomed in micrographs shown in the left panel of Figure 2.6b.

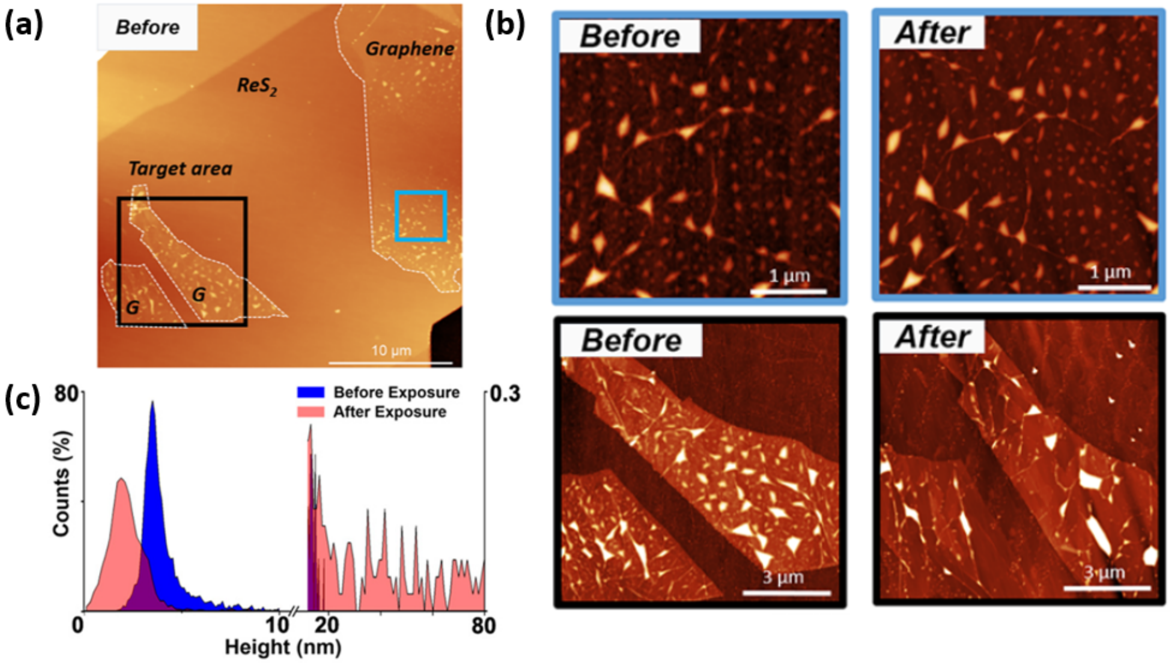

Figure 2.6: (a) AFM micrograph of two independent graphene flakes supported by an ReS$_2$ substrate. A target area is selected, represented by the black box. (b) Zoom in AFM micrographs of the blue box (the unexposed region, top two panels) showing no change in residue morphology, and the black box (the exposed region, bottom two panels) showing significant blister residue diffusion and general sample flattening. (c) Histogram of the AFM pixel height before and after laser exposure in the black box region.

The adhesion energy between a graphene film and its substrate varies for different heterostructures.[65] Therefore, the heat needed to overcome the adhesion energy keeping the blister residues in place also varies depending on the heterostructure. For graphene supported by ReS$_2$, we select a targeted area represented by the black box in Figure 2.6a, program a 532 nm continuous wave laser focused to 1 μm spot to iterate over this path, and find that a power of 8.7 mW is necessary to generate the needed heat to diffuse blister residues, and improve the cleanliness and flatness of the graphene device.

This is demonstrated in the height histogram shown in Figure 2.6c. The distribution of heights is shifted toward 0 nm after exposure (indicating an increase of flattened regions). We also find that only after exposure is there a presence of few tall blisters. This is desirable, because there is an increased region of clean, flat graphene which is necessary for many micron-scale graphene device based experiments. Furthermore, we find that the technique can successfully be applied locally, such that only the chosen targeted area is cleaned, and unexposed graphene remains unchanged. This is seen in the left panel of Figure 2.6b where the targeted areas residue density is reduced, and the non-targeted area remains unchanged.

2.1.3 Metrological characterization

As samples are fabricated in the above methods, we require techniques for metrological characterization that ensures general device suitability for measurements, as well as ensures minimal device to device variation. These metrological tools allow us to inspect the graphene surface's physical structure (with optical microscopy and atomic force microscopy), inspect the graphene thickness and lattice quality (with Raman spectroscopy), and perform electrical transport measurements (using graphene in an FET geometry). The following sections review these techniques, and how they are applied to metrologically characterize samples used in this work.

Optical microscopy

Once samples are prepared, optical microscopy presents a quick way of investigating the success of the transfer. We aim for general continuity of the film (Figure 2.7a) with a minimized amount of tears, wrinkles, or visibly large PMMA residue. Residues such as tears and PMMA can be seen more clearly through a 50x microscope objective as in Figure 2.7b. Graphene films prepared to the quality presented are typical of the CVD wet transfer technique, and are the standard samples used throughout the remainder of this work.

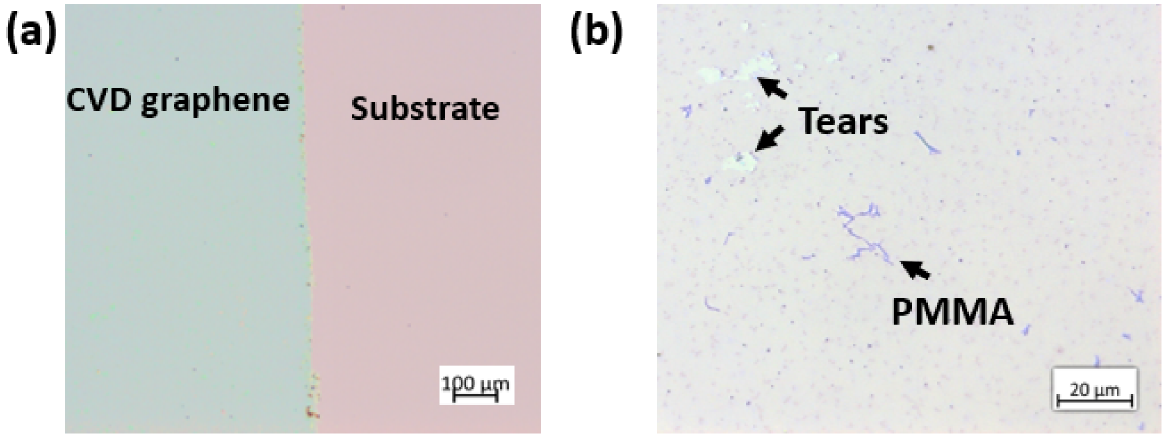

Figure 2.7: (a)5X objective view of transferred CVD graphene. The boundary between graphene and substrate through the middle of micrograph is evident. (b) 50X objective view of CVD graphene. Residues and tears from transfer are indicated.

Atomic force microscopy

Optical microscopy allows us to quickly scan over the entire region of the sample, however atomic force microscopy allows higher spatial resolution of the surface residues, roughness, and height profile of our samples. It allows us to resolve features that are on the order of nanometers, beating the optical diffraction limit considerably. The atomic force microscope works based on the principle of scanning a sharp tip across a surface, and detecting the deflection of the cantilever due to its interaction with the material surface.

AFM probes are typically made from sharply etched silicon, are around 10 nm wide at the tip (Bruker SCANASYST-air) and mounted on a sensitively reflective cantilever. A laser beam is positioned on the cantilever, and the reflected laser beam is collected at a position sensitive detector (PSD) where slight deflections in the beam due to interactions between the sample and tip can be registered. Interactions that can be detected fall into repulsive and attractive categories. There exists three modes of operation each falling into either an attractive or repulsive category (contact mode, tapping mode, and non-contact mode).

Figure 2.8: Operating modes of the tip in atomic force microscopy. (a) **Contact mode**, where the tip makes contact with the material surface and the repulsive force is detected. (b) **Non-contact mode**, where the tip is maintained a distance above the surface, and the attractive force is detected. (c) **Tapping mode**, where the tip is vibrated at a resonant frequency such that it contacts the material at the peak amplitude.

In **contact mode** AFM (as in Figure 2.8a), the tip is brought very close to the surface of the sample until a *repulsive* force is felt. This repulsion is maintained by a feedback loop that consists of a piezo modulating the force whenever a force deflection is felt due to the presence of a height profile. Piezo voltage changes within the feedback loop are stored as the height of features on the material. In **non-contact mode** AFM (as in Figure 2.8b), the tip is brought near the surface of the material, but is not brought into contact so that the dominating force is *attractive* van der Waals. The cantilever is vibrated at a resonant frequency and any changes made to the oscillations (in amplitude, phase, or frequency) are in response to force gradients across the sample due to the presence of surface features. The AFM adjusts the sample-tip distance to correct for changes made due to this attractive force, and the result is again a height profile. Finally, in **tapping mode** (as in Figure 2.8c), the tip is again driven at its resonant frequency, however the amplitude of the oscillations are tuned such that the tip touches the surface of the sample at each oscillation. When the tip touches the surface, the oscillation amplitude is changed however a feedback loop works to maintain a constant amplitude. Changes to the oscillation amplitude provide a means for generating a topographic map.

For the purpose of this thesis, atomic force microscopy of large area graphene and graphene heterostructures was performed in either non-contact mode or tapping mode with either the Park NX-10, or the Bruker - Dimension Icon. These two modes are selected due to their low contact with the graphene surface, minimizing chance of sample destruction.

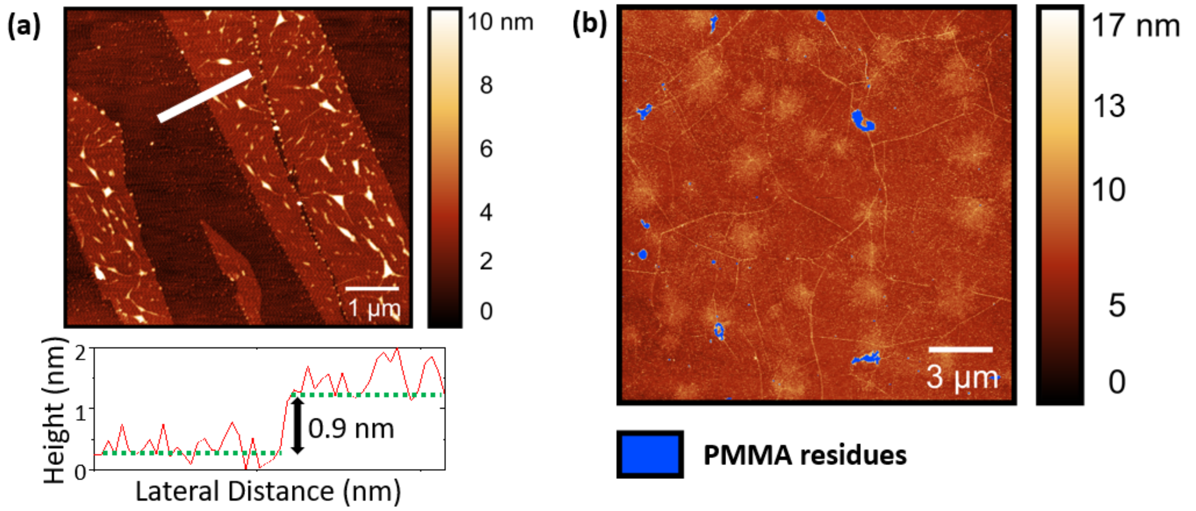

Figure 2.9: Atomic force micrographs of exfoliated graphene flakes on a ReS_2 substrate (a) and large area CVD graphene supported by Si/SiO_2 substrate (b). (a) Surface profile is measured across the white line to measure the height of the graphene flake (0.9 nm). (b) PMMA residues are marked by the purple color to calculate the local density of PMMA residue.

We use AFM maps to measure sample thickness, as in Figure 2.9a. This is useful for confirming the thickness of the sample as either monolayer graphene ($\sim$ 0.7 nm), bilayer graphene ($\sim$ 1 nm), or few layer graphene. We can also use it to locally probe the cleanliness of samples in terms of polymer residue density and separation (as in Figure 2.9b). This can be done by applying a grain mask to the AFM image that selects features with a selected height profile. We can measure the number of features (N), and calculate a 2-D density distribution of residues (assuming that on average residues are $\sim$ the same size).

$$\eta = \frac{N}{A_{tot}} \tag{2.1}$$

where η represents the area density of residues, and A_{tot} represents the total area of the AFM scan. In the case of the sample in Figure 2.9b, $N = 41$ and $A_{tot} = 400\ \mu\text{m}^2$ giving $\eta = 0.1025\ \mu\text{m}^{-2}$. The average separation or distance between residues can be estimated by:

$$l_{avg} = \sqrt{\frac{1}{\eta}} \tag{2.2}$$

where for the sample in Figure 2.9b, $l_{avg} = 3.5\ \mu\text{m}$. For this study we do not select samples based on their measured residue density. The AFM measurement is to give a representative idea of the general residue density using a consistent surface cleaning method. While we assume the general surface has the local residue density measured with AFM, we do not aim to extend it towards a quality control tool.

Raman spectroscopy of graphene

Raman spectroscopy is a useful non-contact tool for characterizing the physical properties of graphene samples used within this work. Through determination of the material's vibrational modes, it gives a compositional fingerprint, and enables the probing of more specific properties including but not limited to, layer thickness,[66] lattice defects,[67] strain,[68] and doping.[69] Spontaneous Raman spectroscopy works by illuminating a material with monochromatic light, typically a laser. The laser photons interact with the material's vibrational modes or phonons, resulting in the photon energies being up or down shifted. More specifically, the light excites electrons in the system to virtual energy states which subsequently relax and return to their original state. This relaxation can be facilitated through a direct transition (elastic scattering), in a process called Rayleigh scattering. Relaxation can also occur through the absorption or creation of a phonon (inelastic scattering), called Stokes or Anti-Stokes scattering. The scattered light from these relaxations is then collected, and observed as Raman peaks on a spectrum. Depending on the vibrational modes in a material (which are dictated by its crystalline or molecular makeup), Raman peaks will appear at specific frequencies with specific intensity, making it an invaluable tool for chemical and structural fingerprinting.

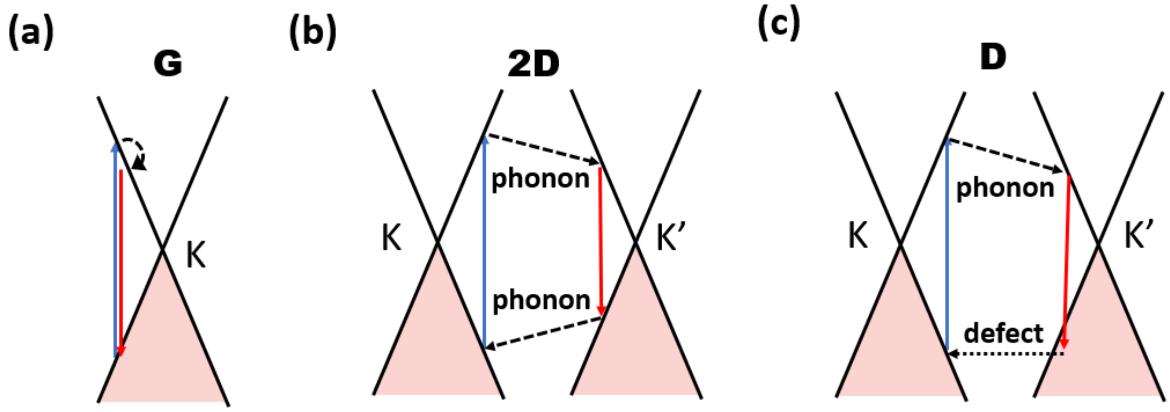

Figure 2.10: Scattering processes within the Dirac cones near the K and K' point that lead to Raman peaks in graphene. Blue arrows represent photon absorption. Red arrows represent photon emission. Phonon wave vectors are represented by a dashed line, and defect scatterers are represented by a dotted line. It is important to note here that Raman processes connect virtual energy states, and while these depicted images illustrate real energy states, they provide an insightful picture to the Raman scattering processes in graphene. (a) 1 phonon intravalley scattering near the K point responsible for the G peak. (b) 2 phonon intervalley scattering process-2D peak. (c) 1 phonon intravalley scattering process-D peak.

In graphene, the signature peaks are the G (1582 cm^{-1}), and 2D (2700 cm^{-1}) peak. In the case of a disordered sample, where defects in the lattice are present or spectroscopy is collected at an edge, a D peak emerges at half the wave number to the 2D peak (1350 cm^{-1}). These peaks originate from the different phonon modes present in the graphene lattice and are typically those used for characterizing graphene.

Within graphene there are 6 normal phonon branches, the G peak originating from the high frequency phonon mode (the E_{2g} mode) near the Brillouin zone center, or Γ point.[70] This peak is also present in bulk graphite. It is the only main peak that originates from a normal first order Raman scattering process, in which *one phonon* facilitates an intravalley photon relaxation (as in Figure 2.10a). The 2D peak originates from a second order Raman scattering process in which *two phonons* with equal and opposite momentum wave vectors facilitate the intervalley photon relaxation near the K and K' points (as in Figure 2.10b). Finally, the D peak originates again from a second order scattering process, however in this case involves a scattering event by one defect and one phonon near between the K and K' points[71] (as in Figure 2.10c).

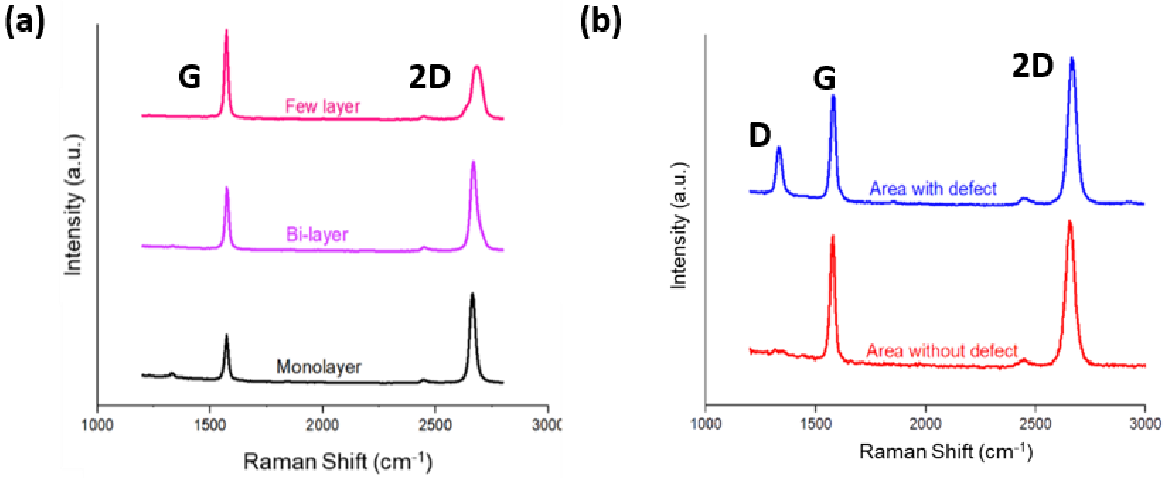

Figure 2.11: (a)Raman spectrum of graphene of different thickness highlighted by color. Monolayer I ($\frac{2D}{G}$) = 2.1 and FWHM (2D) = 30 cm^{-1}. Bilayer I ($\frac{2D}{G}$) = 0.8 and FWHM (2D) = 41 cm^{-1} showing how the FWHM of the 2D peak broadens for increased thickness. Extracted parameters are retrieved by fitting the spectra to Lorentzian functions. (b) Raman spectra showing the emergence of a D peak on a spot of graphene that has a defect within the Raman laser focus. The D peak is centered at 1348.46 cm^{-1}.

In analyzing samples prepared within this thesis (both mechanically exfoliated and large area CVD) we use Raman spectroscopy to locally probe the number of layers, and detect defects at several spots across the samples. This is done by analysing the shape and relative size of the peaks described above in a given spectrum (G, 2D, and D peaks). The thickness of graphene can be inferred by the shape of the 2D peak. As mentioned, for monolayer graphene the 2D peak originates from 2 phonons with equal and opposite momentum near the K point. This scattering process forms an intense, sharp peak at 2700 cm^{-1}. For bilayer graphene the two pairs of Dirac cones overlap, making 4 phonon scattering events possible with slightly different momenta near one frequency. This broadens the 2D peak[70] significantly as thickness is increased. Therefore, the relative height of the 2D and G peak change with the thickness of graphene. For monolayer graphene, the G peak is limited to one intravalley scattering process per K point, while in thicker graphite the overlapping dispersions allow for more intravalley scattering at the same frequency, enhancing the G peak intensity. For monolayer graphene the 2D peak occurs at one frequency resulting in a sharp peak, while in thicker graphite the peak is broadened as described earlier. Therefore, in monolayer graphene the G peak is smaller than the 2D peak, and for thicker graphite the G peak becomes comparable or larger than the 2D peak. More specifically, in monolayer graphene I($\frac{2D}{G}$) ≈ 2, while for bilayer I($\frac{2D}{G}$) ≈ 1 and increasingly smaller for few layer. The effects of 2D broadening described above, and relative height diminishing are seen in Figure 2.11a, where spectra for different thickness are displayed.

Field effect in graphene

As mentioned, graphene films can be straightforwardly incorporated into a field effect transistor geometry,[4,32] and their carrier density and therefore Fermi level tuned by application of a back gate voltage. Such a measurement setup is depicted in Figure 2.12a, where a graphene film is supported by a silicon wafer with 285 nm SiO_2 insulating dielectric to facilitate the application of back gate voltage. The DC resistance of the graphene is probed as the back gate voltage is swept. These types of devices are fabricated readily as described in Section 2.1.1.

The zero-gap band structure of graphene allows both easy tunability of carrier density, and continuous tunability of carrier type; from a hole to electron regime.[28] This tuning is evident in Figure 2.12b, where the resistance of the graphene device increases as electrons are injected into valence bands states. This decreases the density of states of charge carriers, and thereby increases the resistance. In this sample, valence bands states are completely filled to the charge neutrality point at an applied gate voltage of

$V_g = +60$ V, indicating that this sample is strongly p(hole)-doped.

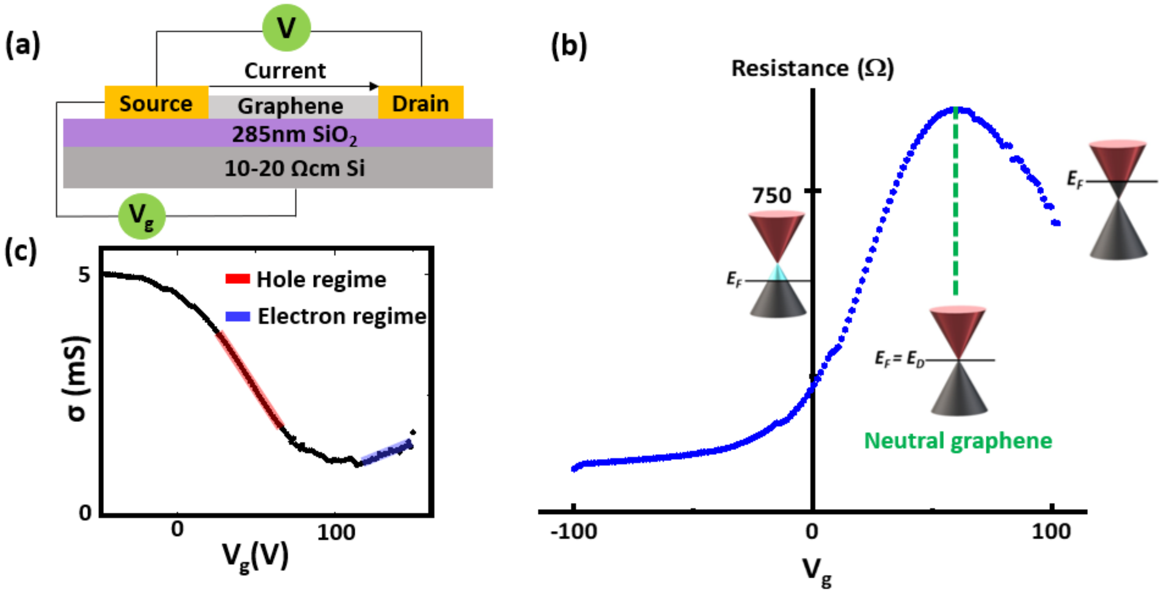

Figure 2.12: (a) Schematic of the 2 point probe device structure used to perform a field effect measurement on graphene. (b) Ambipolar resistance modulation of a graphene film as a function of backgate voltage. The peak of the resistance curve corresponds to the charge neutrality point (CNP), and indicates that at 0 V_g in our devices, graphene films are hole (p) doped. (c) Conductivity as a function of backgate voltage. Hole and electron carrier regimes are highlighted in red and blue respectively.

The carrier density (n_s) in the graphene film is varied, following a linear relationship with gate voltage:[28]

$$|n_s| = \frac{CV_g}{e}, \quad C = \frac{\epsilon_0 \epsilon_r}{t_{ox}}, \tag{2.3}$$

where V_g is the applied gate voltage, e is the electronic charge, C is the gate capacitance per unit area, ϵ_0 is the vacuum permittivity, ϵ_r is the SiO_2 dielectric constant, and t_{ox} is the thickness of the dielectric. For our 285 nm thick SiO_2, the gate capacitance per unit area is 1.21×10^{-8} F/cm^2, and the carrier density can be directly extracted from V_g.

Finally, we can calculate the conductivity (σ) directly from the measured resistance (R) using $\sigma = \frac{1}{R}$. We can then relate σ to the carrier density (n_s) through a proportionality constant typical of semiconductors, the drift mobility (μ). This is done by first recalling that when electric field (E) is applied to a conductor, carriers will acquire an average drift velocity v_d. The conductivity of the material is written as

$$\sigma = \frac{en_s v_d}{E} \tag{2.4}$$

Furthermore, the drift mobility represents a proportionality constant between the acquired drift velocity and the applied field following $\mu = \frac{v_d}{E}$. Therefore, we can substitute μ into Equation (2.4), to relate the drift mobility to both the conductivity and the carrier density

$$\sigma = en_s\mu, \quad \mu = \frac{\sigma}{en_s} \tag{2.5}$$

Finally, we can rewrite Equation (2.5) in terms of the backgate voltage using Equation (2.3).

$$\mu = \frac{t_{ox}}{\epsilon_0\epsilon_r}\frac{\sigma}{V_g} \tag{2.6}$$

Important to note is that the region in which the preceding theory is valid is limited to a diffusive Drude transport regime, or where the conductivity is **linearly dependent** on the carrier density and hence on the gate bias.[4] This region is selected based on linear fitting parameters, and is indicated in Figure 2.12c. In fitting the linear relation between the conductance and the gate bias, the mobility can be extracted directly using Equation (2.6). Furthermore, for samples where both the hole and electron carrier regime are well characterized, one can calculate the hole and electron mobility. The conductivity as a function of gate bias is sometimes asymmetric, leading to hole and electron mobilities that are different from each other. Generally, this asymmetry is attributed to imperfections in the sample, and interactions of graphene with the contact metal.[72] In the case of the sample presented in Figure 2.12b,c the carrier density is measured to be cm^{-2}, and the hole mobility is measured to be 2300 cm^{2}V^{-1}s^{-1}.

2.2 Graphene in the infrared region

While the above described technique presents a reliable way to extract graphene's equilibrium transport properties, it (i) requires the deposition of metal contacts, and (ii) is highly invasive to the graphene. Furthermore, the question of how contacting graphene with foreign materials affects the carrier properties is difficult to address. For example, it has been shown that graphene devices with 'more invasively designed' contacts (probes that cross the whole graphene sheet) exhibit a strong electron-hole asymmetry.[73] It was also found that graphene devices with metal contacts that have low adhesion strength (aluminum, for example) exhibited pronounced electron-hole asymmetry.[74] Overall, the electrical characterization technique contributes to breaking graphene's local spatial charge homogeneity (altering the intrinsic properties being measured). Furthermore, it is not a high-throughput or scalable technique for characterizing large area films in a efficient time frame. Finally, metal deposition renders the graphene sample useless to alternate applications post characterization. The remainder of this thesis is dedicated to describing the implementation of a non-invasive, non-contact characterization technique that allows for complete extraction of graphene's transport properties, without deposition of metal leads. This optical based technique also offers the future potential of being scalable within an industrial characterization setting,[75] and does not damage the sample.

2.2.1 Optical spectroscopy to probe carrier dynamics

Optical measurements offer the advantage of probing material properties without making physical contact. For graphene, optical measurements are an invaluable tool for studying the band structure[76] as carriers interact with radiation across the electromagnetic spectrum. Optical interactions in graphene can be broadly categorized into one of two groups, interband absorption and intraband absorption.[77,78] The dynamics that govern how radiation across the infrared regime interacts in graphene is summarized in Figure 2.13.

Interband optical absorption

Interband absorption events arise due to direct transitions between the valence and conduction bands[79] (as shown in the left panel of Figure 2.13) from photons with high enough energy. For graphene's band structure, photons with energy 1000's meV satisfy this process, falling between the visible and near infrared region. The conductivity due to such transitions is found to be frequency independent within the linear dispersion regime of graphene, and is written as $\sigma(\omega) = \frac{\pi e^2}{2h}$.[28,78,80–82] This results in the well known constant absorbance of graphene across the visible and near-infrared spectrum $\mathrm{A}(\omega) = \pi\alpha = 2.29\%$, where α is the fine structure constant.[19,79]

The frequency independent behaviour does not hold for all photon energies, as seen in Figure 2.13. As the optical wavelengths increase, both the energy of the photons inducing the transitions and the conductivity decrease. This indicates that no interband transitions can take place and therefore absorption events are blocked. This absorption blocking is called Pauli blocking and is due to free carriers (fermions) occupying all available energy states in the sample.[83,84] The Fermi level is tuned away from the Dirac point, and photon energies of at least $2\mathrm{E}_F$ are required to make an interband transition, as transitions from empty states are not possible.[79] This effect has been studied in samples where the graphene is gated,[85,86] or chemically doped[84] to tune the Fermi level, and the onset of Pauli blocking shifts.

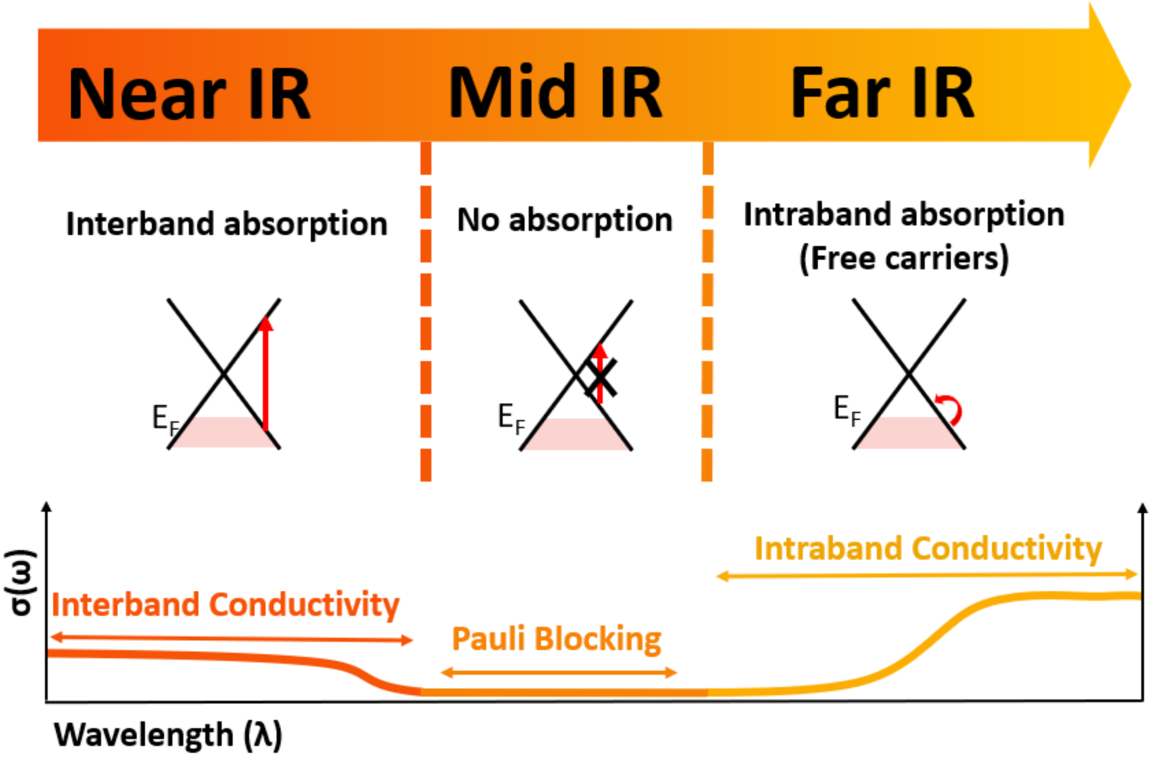

Figure 2.13: Left panel: Direct, frequency independent transitions between valence and conduction bands giving rise to a constant interband conductivity. This is valid within the tight binding model, for transitions with energy where the Dirac cone approximation is valid. Middle panel: Transitions are prohibited due to Pauli blocking. Photon energy is not tuned to promote a transition, and transitions can not be made from empty states. Right panel: Low frequency transitions that conserve momentum by scattering with a phonon or defect, giving rise to a Drude like intraband conductivity.

Intraband optical absorption

Finally, intraband absorption events arise due to indirect transitions within the conduction or valence band from low energy photons. Within this picture direct absorption of a photon by an intraband transition does not satisfy conservation of momentum, and requires extra scattering with a phonon or defect. This scattering picture is visualized in the right panel of Figure 2.13, and for graphene's band structure photon energies that satisfy this process fall in the far infrared or terahertz region. The scattering processes and carrier motion in this region result in an absorption peak that is very pronounced as the many free carriers in doped graphene interact with the low energy photons. Furthermore, the frequency dependent conductivity has a Drude form, as carriers undergo intraband transitions and experience scattering events to conserve momentum.[19,24,81,87]

Describing carrier interactions in large area graphene using the Drude model has proven to be successful in the THz region, confirming the dominance of intraband over interband conductivity at far-infrared frequencies. Currently the Drude model is standardly applied to THz conductivity spectra for extraction of graphene transport properties. The technique has been widely applied in terahertz mapping technologies to non-invasively characterize large area graphene films, including those covering entire 4 inch wafers,[20,88] and those covering 30 cm wide polymer films.[89] THz spectroscopy has also been applied to large area graphene devices that are simultaneously gated, allowing for transport properties to be measured as a function of variable Fermi level.[75,90] Furthermore, a tunable terahertz modulator was demonstrated based on a graphene gate biasing geometry. The density of available intraband transitions is tuned using the gate bias, allowing for finely controlled THz signal attenuation.[91] This functionality could be useful for future THz based opto-electronic devices that require the ability to manipulate THz electromagnetic waves.

2.2.2 Drude model for free carrier dynamics

The Drude model for the dynamics of carriers in metals and doped semiconductors is successful in describing their response to low energy radiation. Furthermore, it has been shown to very accurately model intraband carrier behaviour in the famously non-classical material, graphene, despite the Drude model being based on classical physical principles.

In its original form, Drude applied the kinetic theory of gases to carriers in a metal, an effective ‘gas of electrons’.[92,93] The model assumes that the system is comprised of completely free and independent carriers moving randomly between elastic scattering events. It assumes that scattering events are due to interactions with randomly positioned stationary ionic cores, and happen with an average time interval τ between collisions.

We can calculate the motion for an electron under a spatially homogeneous time varying electric field (in our case the THz field pulse) based on the classical equation of motion:

$$\frac{d\mathbf{p}}{dt} = -\frac{\mathbf{p}(t)}{\tau} - e\mathbf{E}(t) \tag{2.7}$$

where $\mathbf{E}(\mathrm{t}) = \mathrm{Re}(\mathbf{E}(\omega)\mathrm{e}^{-i\omega t})$, and represents the time varying field. We seek a steady state solution of the form $\mathbf{p}(\mathrm{t}) = \mathrm{Re}(\mathbf{p}(\omega)\mathrm{e}^{-i\omega t})$, where $\mathbf{p}(\mathrm{t})$ represents the average momentum of the disturbed electron. Substituting $\mathbf{E}$ and $\mathbf{p}$ into Equation (2.7) becomes

$$-i\omega\mathbf{p}(\omega) = -\frac{\mathbf{p}(\omega)}{\tau} - e\mathbf{E}(\omega) \tag{2.8}$$

Solving for $\mathbf{p}$ we find $\mathbf{p}(\omega)$ = - $e\tau\mathbf{E}(\omega)/(1 - i\omega\tau)$. To relate this momentum to the complex conductivity, we recall that the classical momentum of a carrier is related to its velocity by $\mathbf{p} = m^* v$, where m^* is the effective mass of the charge carrier, and v is the carrier velocity. The current density is then given as $\mathbf{j} = nev$ = - $ne\mathbf{p}(\omega)/m^*$, where n is the density of carriers in the material. It can be written in terms of $\mathbf{E}(\omega)$ as:

$$\mathbf{j}(\omega) = -\frac{ne\mathbf{p}(\omega)}{m^*} = \frac{ne^2\tau\mathbf{E}(\omega)}{m^*(1 - i\omega\tau)} \tag{2.9}$$

The current density is also directly proportional to the electric field $\mathbf{E}(\omega)$ in the material, through a proportionality constant known as the complex frequency dependent AC conductivity, $\tilde{\sigma}(\omega)$.

$$\mathbf{j}(\omega) = \tilde{\sigma}(\omega)\mathbf{E}(\omega) \tag{2.10}$$

We therefore write for the electron $\tilde{\sigma}(\omega)$

$$\tilde{\sigma}(\omega) = \frac{\sigma_{DC}}{1 - i\omega\tau}, \quad \sigma_{DC} = \frac{ne^2\tau}{m^*} \tag{2.11}$$

where σ_{DC} represents the conductivity at $\omega = 0$. This function describes a complex Lorentzian, as shown in Figure 2.14.

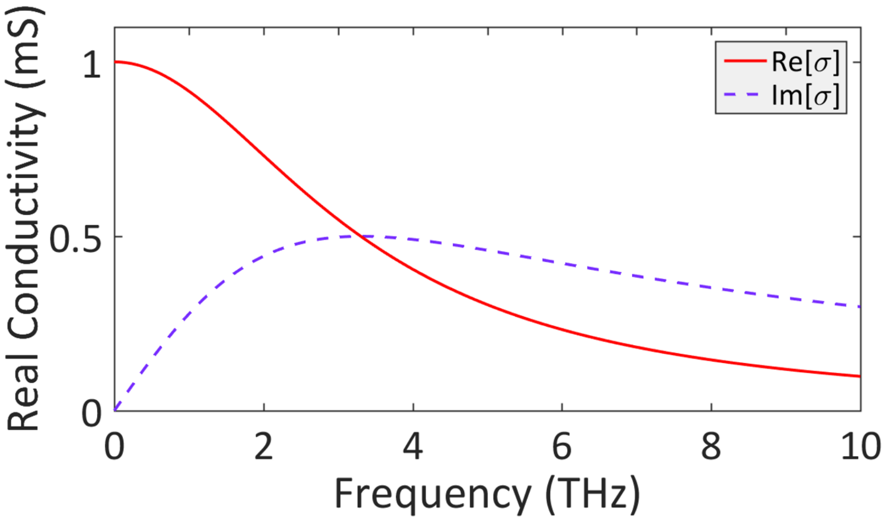

Figure 2.14: Real (solid) and imaginary (dashed) parts of the Drude conductivity. The real part is a Lorentzian centered at $\omega = 0$ THz with a peak value equal to σ_{DC} (1 mS). The y-axis is not normalized. Re(σ) crosses Im(σ) at $\omega = 1/\tau$ (inverse scattering time) or Γ (the scattering rate).

As mentioned, the Drude formalism works well for metals and semiconductors where m^* is the band mass in a classical dispersion such as in $\epsilon(\mathbf{k}) = k^2/2m^*$. The electrons in graphene however, are massless Dirac fermions, and require a more general approach (semi-classical Boltzmann transport theory) to calculating their conductivity. This approach will allow us to take the two-dimensionality and conical band structure into account, and nevertheless will recover the general Drude like spectral shape as alluded in Equation (2.11).

The Boltzmann expression for the conductivity in three dimensions is written as[93]

$$\sigma(\omega) = Ne^2 \int \frac{d\vec{k}}{(2\pi)^3} \frac{v^2(\vec{k})}{3} \frac{1}{1/\tau(\epsilon) - i\omega} \left(-\frac{\partial f(\epsilon)}{\partial \epsilon} \right) \tag{2.12}$$

where N is the degeneracy of spin and valley states, $v(\vec{k})$ is the carrier velocity, and f is the Fermi distribution function. For a system with parabolic dispersion, $v^2(\vec{k}) = 2\epsilon/m^*$. Furthermore, using the known relation for transitioning from wave vector to energy integration space

$$N \int \frac{d\vec{k}}{(2\pi)^d} = \int d(\epsilon) g(\epsilon) \tag{2.13}$$

where d is the dimensionality of the space, and we can make a change of variables to integrate the conductivity[94] in terms of ϵ

$$\sigma(\omega) = \frac{2e^2}{3m^*} \int d(\epsilon) g(\epsilon) \epsilon \frac{1}{1/\tau(\epsilon) - i\omega} \left(-\frac{\partial f(\epsilon)}{\partial \epsilon} \right) \tag{2.14}$$

We note that the degeneracy of the spin and valley states is taken care of inside the final density of states, $g(\epsilon)$ for the materials considered here. For metals, the Fermi energy is typically between 1-10's of eV, much larger than the thermal energy at room temperature (0.0258 eV), and the Fermi distribution can be approximated as a step function where $(-\frac{\partial f}{\partial \epsilon}) \approx \delta(\epsilon - \epsilon_F)$ making Equation (2.14) straight forward to integrate

$$\sigma(\omega) = \frac{2e^2}{3m^*} \epsilon_F g(\epsilon_F) \frac{1}{1/\tau(\epsilon_F) - i\omega} \tag{2.15}$$

Finally, for electrons in such a 3D parabolic dispersion, the density of states at the Fermi level is given[23,94] $g(\epsilon_F) = 3n/2\epsilon_F$, and the conductivity reduces to the familiar form

$$\sigma(\omega) = \frac{\sigma_{DC}}{1 - i\omega\tau}, \quad \sigma_{DC} = \frac{ne^2\tau}{m^*} \tag{2.16}$$

For massless Dirac fermions in graphene, this derivation requires more attention, the carrier velocity is independent of momentum $v(\vec{k}) = \hbar^{-1}(\partial\epsilon/\partial k) = v_F = 1.1 \times 10^6$ m/s also called the Fermi velocity. The Boltzmann expression for the conductivity written in terms of this carrier velocity is then

$$\sigma(\omega) = Ne^2 \int \frac{d\vec{k}}{(2\pi)^2} \frac{v^2(\vec{k})}{2} \frac{1}{1/\tau(\epsilon) - i\omega} \left(-\frac{\partial f}{\partial \epsilon}\right) = \frac{Nv_F^2 e^2}{2} \int \frac{d\vec{k}}{(2\pi)^2} \frac{1}{1/\tau(\epsilon) - i\omega} \left(-\frac{\partial f(\epsilon)}{\partial \epsilon}\right) \tag{2.17}$$

where the factor 1/3 has become 1/2 to reflect the 2-dimensionality of the system. In this case, we cannot use the step function approximation for the Fermi distribution, as the Fermi level can become comparable to the thermal energy ($\approx$ 26 meV) in graphene. Instead we use the typical representation of the Fermi distribution given by[95]

$$f(\epsilon) = \frac{1}{exp[\frac{\epsilon-\mu_c}{k_B T}] + 1}, \quad -\frac{\partial f(\epsilon)}{\partial \epsilon} = \frac{1}{k_B T} \frac{exp[\frac{\epsilon-\mu_c}{k_B T}]}{(exp[\frac{\epsilon-\mu_c}{k_B T}] + 1)^2}, \tag{2.18}$$

where μ_c is the chemical potential, k_B is the Boltzmann constant, and T is the temperature. The integral over momentum can then be replaced in integration over energies using Equation (2.13), with the density of states for graphene given as $g(\epsilon) = \frac{2\epsilon}{\pi(\hbar v_F)^2}$. The final conductivity for graphene within the conical dispersion region is then

$$\sigma(\omega) = \frac{2e^2 k_B T}{\pi\hbar^2} ln\left(2\cosh\left(\frac{\mu_c(T)}{2k_B T}\right)\right) \frac{1}{1/\tau - i\omega} \tag{2.19}$$

The classical Drude spectral shape is conserved as can be seen in the far right side of Equation (2.19), with only the front pre-factor changed. This new pre-factor is known as the Drude weight, and in the limit of $k_B T \ll \mu_c$, can be reduced to $\mu_c e^2/\pi\hbar^2$.[96] Furthermore, the chemical potential is determined by the carrier concentration as $\mu_c = \hbar v_F \sqrt{\pi n}$[97] and we can write a simplified conductivity spectrum that is once again reminiscent of the original Drude form:[19,24,81,87,98]

$$\sigma(\omega) = \frac{\sigma_{DC}}{1 - i\omega\tau}, \quad \sigma_{DC} = \frac{v_F e^2 \sqrt{n}\tau}{\hbar\sqrt{\pi}} \tag{2.20}$$

This result is distinctly different than in classical materials, where the pre-factor, or Drude weight, depends on the carrier mass, and is linearly dependent on the carrier density (n). Therefore, for low energy excitations that induce intraband absorption events (within the far-infrared/terahertz region), the resulting scattering process of carriers and conductivity can be understood within the Drude model outlined above, and for two dimensional graphene, is written as in Equation (2.20).

Chapter 3

Experimental techniques: Terahertz spectroscopy

3.1 Introduction

THz spectroscopy is based on the generation and detection of time resolved pulses of radiation, typically picoseconds long, in the terahertz region of the electromagnetic spectrum. These frequencies lay between electronic (microwave) and photonic (far IR) regions, and are typically estimated to span (0.1-10) THz, 3 mm to 30 μm, or (0.4-40) meV[99] (Figure 3.1). The region has historically been referred to as "the THz gap" due to a lack of suitable tools for generation and detection.[100] On the lower end of the frequency range, electronics based microwave sources and detectors are readily available (from GPS to microwave ovens). On the higher end infrared optical sources and sensors are a well developed family of technologies (from remote controls to night vision).

Despite the challenges presented with a "THz gap", there exists numerous interesting physical phenomena whose time dependent dynamics lay within the sub-picosecond range. These sort of dynamics are well suited to THz spectroscopy since $\omega\tau \approx 1$ (where ω is the angular frequency, and τ is the dynamic time-scale). Applications range from probing vibrational and rotational states of large molecules,[101] to exciton transitions,[102] to optical and acoustic phonon modes,[103] to free carrier dynamics in semiconductor solid state systems.[104] Furthermore, as mentioned in Section 2.2.1 the relevant energy scales for probing free carrier dynamics and intraband transitions in graphene lie in the THz range.

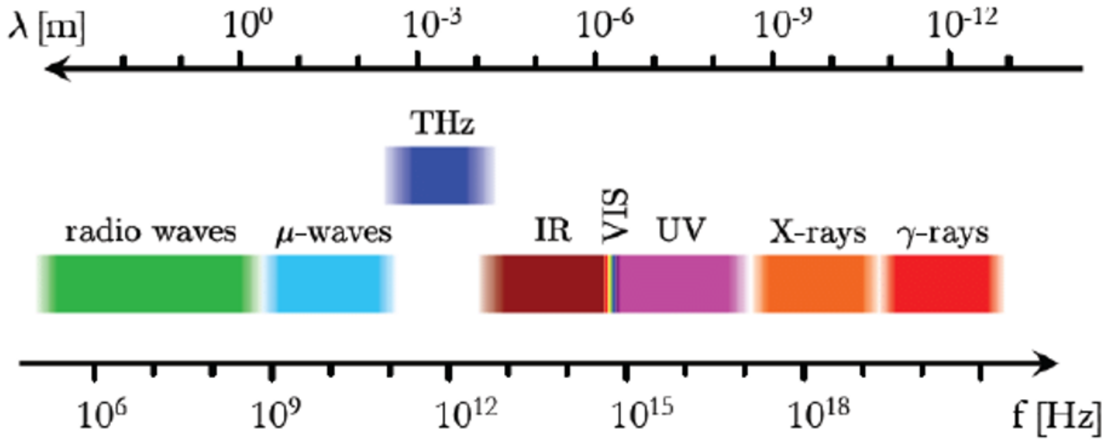

Figure 3.1: Electromagnetic spectrum with THz region highlighted indigo.

With the goal of accessing these dynamics, THz-spectroscopy became increasingly feasible as table top optical sources (in the VIS and NIR) with femtosecond pulse duration (10^{-15}s), intense enough to induce nonlinear behavior in solids became available to researchers.[105] This enabled scientists to irradiate crystals with light intense enough to non-linearly perturb the material optical response, and generate new frequencies, in particular those tuned to the low energy THz region. Emitted radiation in this picture, (with the correct phase matching conditions applied) manifests as freely propagating short electromagnetic pulses.

One advantage of THz spectroscopy over traditional spectroscopies is the ability to directly measure the time resolved oscillating electric field, rather than just the intensity. This allows the collection of the original pulse, and the complex information stored within it, that being the amplitude *and* the phase. Such information allows the spectoscopist to measure the complex optical properties such as the refractive index and conductivity in a single shot measurement, without the use of Kramers-Kroenig relations.

Today THz spectroscopy is a large but ever growing field of science. Highly sensitive spectroscopy in the THz regime is widely accessible in compact table top systems through generation and detection of coherent, freely propagating THz pulses in nonlinear crystals.[106,107] The field continues to evolve, from the implementation of fibre-coupled THz systems[108] to the study of intense THz fields manipulating solid state systems,[109] to the demonstration of THz near field/single pixel imaging,[110] it has experienced tremendous progress since inception, and continues to show increasingly relevant promise.[111]

This section of the thesis will outline the specific techniques used in our lab to generate and detect THz radiation by nonlinear optical methods, allowing us to perform time-resolved terahertz spectroscopy. It will review the theory of difference frequency mixing in a second order nonlinear crystal for THz generation, and the application of electro-optic sampling for its detection. Finally this section will cover the specific optics and electronics used in our THz setup, as well as the physical geometry and theory for measuring optical properties of graphene using THz-transmission spectroscopy.

3.1.1 THz generation by optical rectification

As mentioned, the generation of terahertz radiation is based on the use of ultrashort (100's of fs) infrared pulses down converted to the THz regime using difference frequency mixing. A simplified picture of this second order nonlinear process, also called optical rectification, can be applied to develop an intuition for the workings of THz generation applied within this work. We begin by recalling that the polarization of a material can be written as a power series expansion of the electric field as (assuming that the polarization response is instantaneous with the applied field):

$$P(t) = \epsilon_0(\chi^{(1)}E(t) + \chi^{(2)}E^2(t) + \chi^{(3)}E^3(t) + ...), \tag{3.1}$$

where ϵ_0 is the permittivity of free space, and $\chi^{(n)}$ is the n^{th} order susceptibility of the material. Generally, a material cannot polarize instantaneously due to causality, and the polarization must be written in terms of $E(t')$, making $\chi^{(n)}(t-t')$ time dependent. For the purpose of this thesis, the instantaneous response is sufficient to describe the general THz generation and detection schemes. In linear optics, only the first order contribution is important, however as the field strength of the light becomes more intense, higher order contributions become relevant in describing the polarization.[112] We define intense to be the condition of the field strength approaching the order of the atomic electric field strength ($E_{at} = \frac{e}{4\pi\epsilon_0 a_0^2} = 5.14\times10^{11}$ V/m). $\chi^{(2)}$ is then on the order of

$$P^{(2)} \approx P^{(1)}, \quad \chi^{(2)} \approx \frac{\chi^{(1)}}{E_{at}} \approx \frac{1}{E_{at}} \approx 1.95 \times 10^{-12}\mathrm{m/V} \tag{3.2}$$

Today, the optical intensities accessible by regenerative amplifier laser sources are *easily* able to induce nonlinear effects. For our purposes the second order term is the most important, as it allows for second harmonic generation, and sum/difference frequency mixing. To achieve second order effects a material with a non-zero $\chi^{(2)}$ susceptibility is needed, as the material polarization must be altered under inversion processes. This requires use of a crystal that lacks inversion symmetry, i.e. a crystalline axis that is non-centrosymmetric in structure. In such a crystal, coupled with intense laser pulses, second-order nonlinear processes become possible, and with the proper phase matching conditions, become efficient. In this work we use the nonlinear crystal gallium phosphide, and exploit its $\chi^{(2)}$ susceptibility to generate difference frequency mixing.

If we consider the electric field from the laser amplifier to be of the form:

$$E^n(t) = E_0^{(n)}\cos(\omega_n t) \tag{3.3}$$

and consider a simplified picture such that there are only two frequency components in the amplifiers spectrum (ω_1, ω_2), from Equation (3.1), the second order induced polarization becomes:

$$P^{(2)}(t) = \epsilon_0 \chi^{(2)} E_0^{(1)} E_0^{(2)} \cos(\omega_1 t) \cos(\omega_2 t) \tag{3.4}$$

$$P^{(2)}(t) = \frac{\epsilon_0 \chi^{(2)} E_0^{(1)} E_0^{(2)}}{2} [\cos(\omega_1 - \omega_2)t) + \cos(\omega_1 + \omega_2)t)] \tag{3.5}$$

using the standard trigonometric relation $\cos(x)\cos(y) = \frac{1}{2}[\cos(x-y) + \cos(x+y)]$. Now there is a new established nonlinear polarization that oscillates at either the sum or difference of the two frequencies. Knowing that the nonlinear polarization of a medium acts as a source term for electromagnetic waves by Maxwell's equation

$$\nabla^2 E_{THz} - \frac{n^2}{c} \frac{\partial^2 E_{THz}}{\partial^2 t} = \frac{1}{\epsilon_0^2 c^2} \frac{\partial^2 P^{NL}}{\partial^2 t} \tag{3.6}$$

it is straight forward to see how this induced oscillating polarization generates new electromagnetic waves that oscillate at $(\omega_1 + \omega_2)$ and $(\omega_1 - \omega_2)$. Mixed frequencies fall into one of two cases: (i) $\omega_1 = \omega_2$, where the result is a DC polarization $(\omega_{tot} = 0)$, or a frequency doubled source, called second harmonic generation $(\omega_{tot} = 2\omega)$, or (ii) $\omega_1 \neq \omega_2$, where the result is a source at any sum or difference frequency between ω_1 and ω_2 (sum or difference frequency generation). Figure 3.2 visualizes the simplified difference frequency mixing picture for a pulse in the NIR. Figure 3.2a shows the process from the source spectral amplitude perspective, and Figure 3.2b depicts the same process but from an energy level diagram perspective.

In practice each amplifier pulse does not contain two discrete frequencies, rather a continuous spectrum of frequencies, each arbitrary component interacting with the other. In this thesis, the amplifier pulse is centered at 1035 nm (comfortably in the NIR), with a temporal duration < 100 fs corresponding to a frequency bandwidth of 6 THz. Furthermore, it is important to note that the simplified picture described above

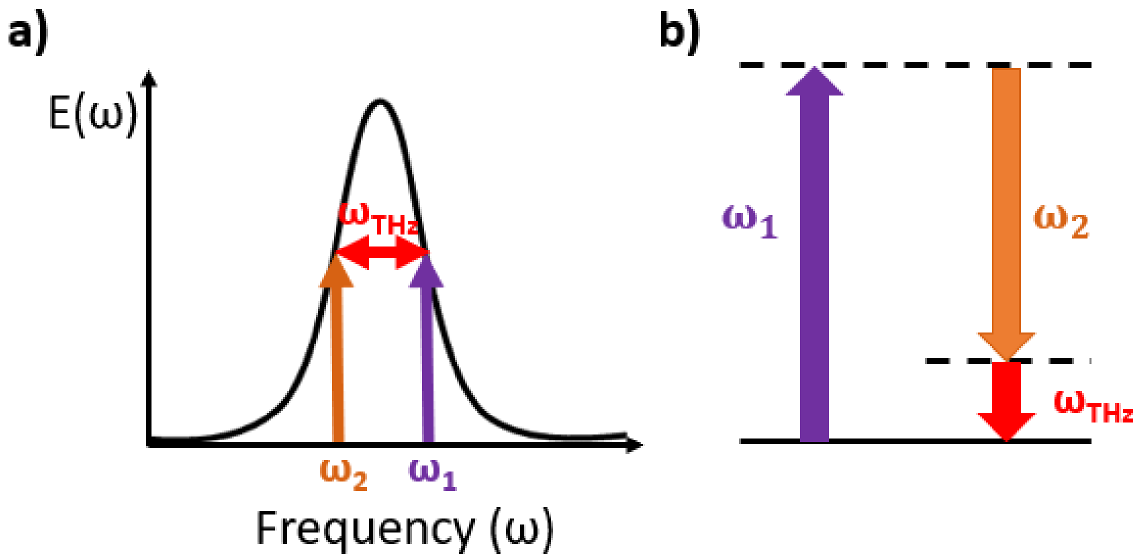

Figure 3.2: **(a)** Laser pulse visualization of difference frequency mixing in nonlinear crystal **(b)** Energy level diagram for visualization of difference frequency mixing.

grossly overestimates the experimentally attainable bandwidth. This picture does not include phase mismatching effects that arise from the co-propagation of the amplifier pulse and the generated THz pulses.

3.1.2 THz detection by electro-optic sampling

Likewise to generation, THz detection is based on the clever implementation of optical effects in non-centrosymmetric media, namely the linear electro-optic 'Pockels' effect. The Pockels effect describes the change in refractive index in a non-centrosymmetric crystal induced by the presence of a static electric field.[113] More specifically, a birefringence is induced resulting in the modulation of the crystals ordinary and extraordinary indices of refraction (n_o and n_e respectively), proportional to the comparatively DC electric field.

Since the duration of the THz pulse is much longer than the duration of the NIR pulse (few ps to $\sim$ 100 fs difference) the THz field appears quasistatic to the NIR, altering it's birefringence proportionally to THz field strength. Therefore, when the NIR gate pulse and THz pulse arrive simultaneously, the polarization state of the NIR is altered in proportion to the THz field strength. More specifically, it causes a phase retardation between the linear polarization components of the gate pulse. By measuring this quantifiable change in the NIR polarization state, the THz field can be measured at one point in time, and by moving the temporal overlap of the two pulses with a delay stage, the entire THz field can be mapped out. This technique is visualized in Figure 3.3 where the dynamics of the scheme are pictured for three different THz-NIR temporal overlaps.

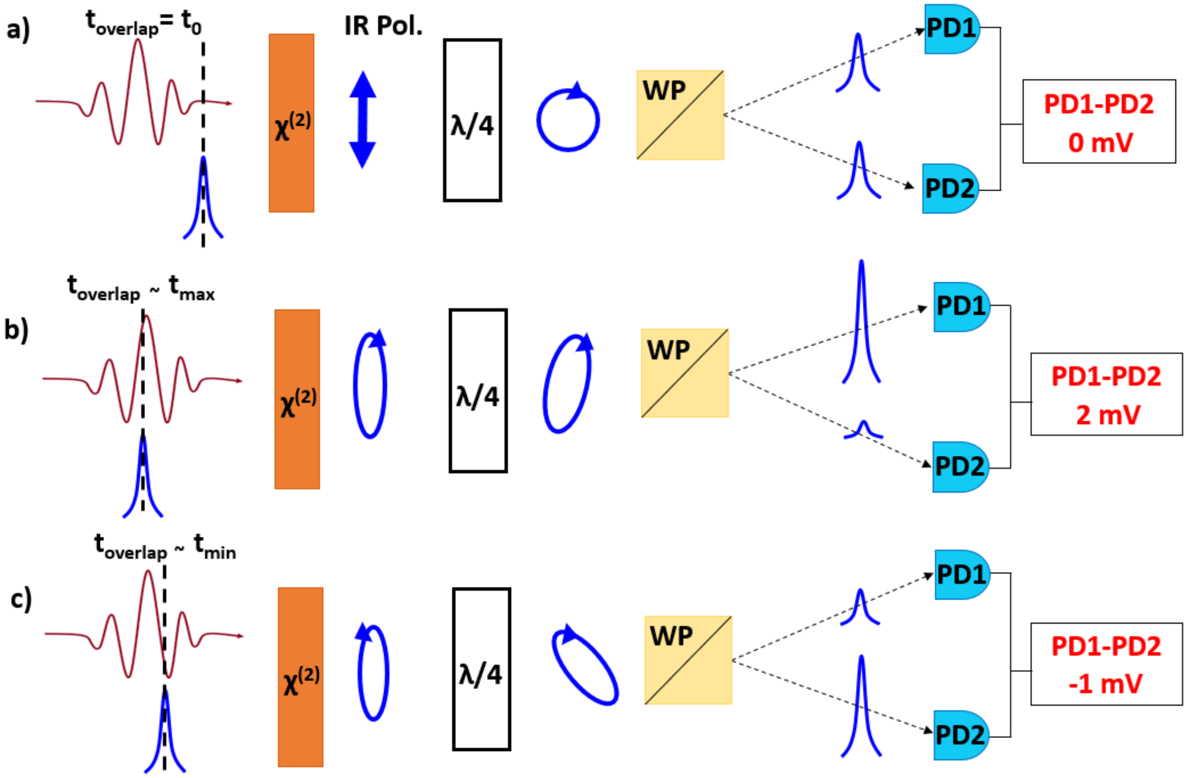

Figure 3.3: Electro-optic sampling for detection of a perturbing THz field. (a) In the absence of an electric field the horizontally polarized gate pulse passes through the unaltered nonlinear crystal. A quarter-waveplate is set to produce circularly polarized light, giving equal contribution to horizontal and vertical polarization. The Wollaston prism separates the components onto two photodiodes, and their difference is measured as 0 mV. (b) & (c) If the gate pulse and the THz pulse temporally overlap the THz field modifies the birefringence in the nonlinear crystal, altering the polarization state of the gate pulse. In this case elliptically polarized light is produced, resulting in a difference in intensity on the diodes proportional to the THz field.

The change in polarization is measured using an ellipsometer consisting of a quarter-waveplate, a Wollaston prism and a pair of photodiodes. The quarter-waveplate is used to initially calibrate the scheme in the absence of a THz pulse. It compensates for any equilibrium birefringence in the nonlinear crystal, circularizing the gate pulse and ensuring the detector output is zeroed when there is no THz-NIR field overlap. The Wollaston prism spatially separates the horizontal and vertical components of the NIR pulse, which can then be detected by the two photodiodes, and the potential difference between them measured. Since the quarter-waveplate balanced the detectors in the absence of the THz pulse, any potential difference measured between them is directly proportional to the THz field at a given temporal overlap with the NIR pulse.

3.2 Experimental setup

The two processes described above for generating and detecting THz radiation were applied to realize the time-domain terahertz spectrometer employed in this thesis. The setup in our lab is depicted in Figure 3.4. An Yb:KGW amplified laser source drives the setup, and the amplified output pulse is centered at 1035 nm, is 180 fs long, has an average power of 2.1 W, and a repetition rate between 1 kHz and 1.1 MHz, tunable by the lasers internal electronics software. The output is guided to an 80/20 beamsplitter, where the pulse is separated along two beam paths.

The highest intensity NIR pulse is lead to the generation arm after passing through a chopper wheel (which enables lock in detection), where it is focused on a non-centrosymmetric medium with a $\chi^{(2)}$ susceptibility. In our case this medium is a gallium phosphide (GaP) crystal. The intense pulse in this nonlinear crystal initiates the optical rectification process as described in Section 3.1.1, generating a pulse of terahertz radiation typically about 2 ps long and containing spectral content between 0-6 THz. The THz pulse diverges outward from the emitter crystal in all directions, and is re-collected and collimated by a parabolic mirror. A germanium wafer is placed in the centre of the beam path to allow transmission of the generated THz, and to block any residual NIR pump light. The pulse is then introduced to another parabolic mirror identical to the first, to bring the THz frequency components to a spatial focus, typically between 0.5 and 1 mm in width. The sample of interest is placed at this focus, and the transmitted pulse is reintroduced to an identical parabolic mirror pair to refocus it into a second GaP detection crystal for THz detection. Finally, we note that due to the high absorption of THz by humidity in the air, all components that involve the THz radiation are contained within a plexiglass box that is purged with dry air (N_2). This ensures the measurements are not affected by water absorption lines.

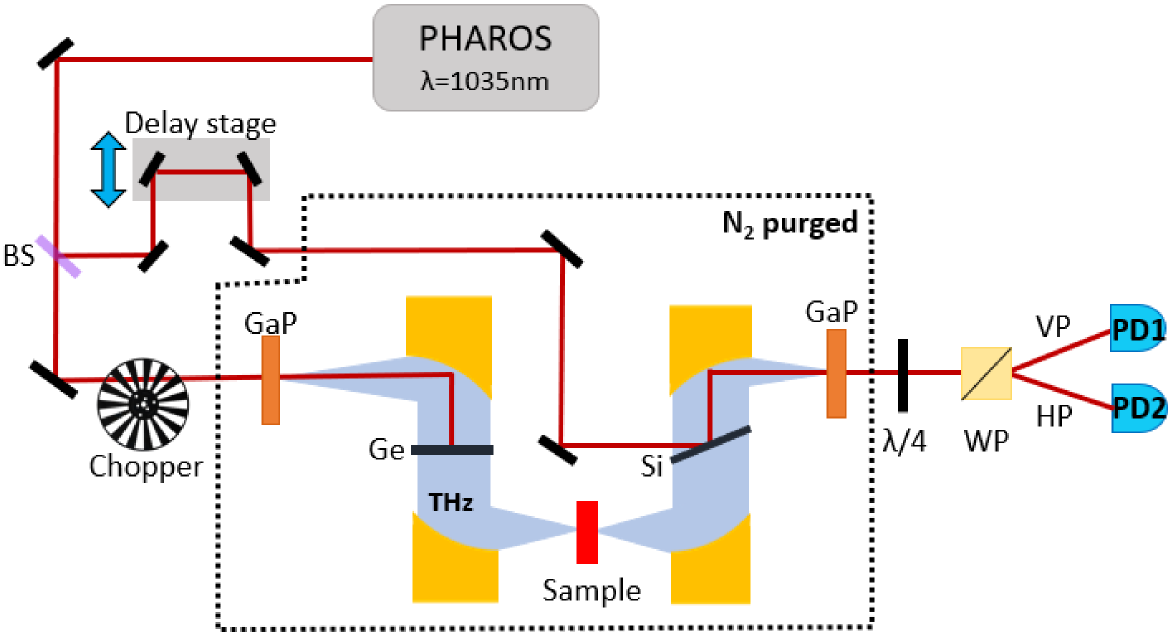

Figure 3.4: Schematic of our terahertz spectrometer. BS: 80/20 beamsplitter, GaP: gallium phosphide, Ge: germanium wafer, Si: silicon wafer, $\lambda/4$: quarter wave plate, WP: Wollaston prism, VP/HP: vertical/horizontal polarization, PD1/PD2: photodiodes.

The NIR pulse with lower intensity is lead to the THz detection or ‘gating’ arm. The first optics it encounters is a pair of mirrors mounted on a motorized translation stage. The NIR pulse is then reflected off a silicon wafer, bringing it back into the generation arm beam path. It is focused with the fourth parabolic mirror into the GaP detection crystal where it is spatially recombined with the THz wave and can act as a gating pulse for electro-optic sampling. Since the optical path of the THz wave is fixed, the temporal overlap of the THz and NIR can be tuned by translating the motorized delay stage and tuning the optical path of the NIR pulse. By scanning the NIR pulse over the temporal range of the THz pulse in the GaP crystal, electro-optic sampling for THz detection can be performed as described in Section 3.1.2. The delay stage used within this work moves in steps of 10 μm, giving $\sim$30 fs temporal resolution in the THz transient.

Finally, THz detection is done through amplified lock in detection, where the input signal (oscillating at the chopper frequency, ω_c) from the photodiodes is multiplied with a reference signal delivered by the local oscillator in the LIA (also selected to oscillate at ω_c). A low pass filter is applied to this product signal, thereby isolating the signals oscillating at ω_c and rejecting signal at all other frequencies (noise). This allows for the detection of weak signals, in high noise backgrounds.

Overall, this scheme allows one to measure the direct terahertz field as a function of delay stage time, facilitating spectroscopy that is phase and amplitude sensitive, and allowing for full extraction of complex material properties, as I will describe in detail in the following section.

3.3 Measuring optical properties with THz transmission spectroscopy

In the time domain spectroscopy setup described in Section 3.2, we collect the electric field, $E(t)$ of the THz pulse transmitted through a sample of interest. This pulse contains both the phase ϕ and amplitude $|E_0(\omega)|$ information. By application of a Fourier transform (via a Fast Fourier Transform algorithm in MATLAB), these properties as a function of frequency can be obtained, allowing for the extraction of complex frequency dependent properties. We write the THz wave in the following way for the remainder of this section.

$$\mathbf{E}(\omega) = E_0(\omega)e^{i\phi} \tag{3.7}$$

where $\phi = n\omega l/c$, and n, l, and c are the refractive index, the thickness of the material, and the speed of light, respectively. In transmission spectroscopy, one needs to collect a THz transient such as one in the form of Equation (3.7) that has passed through the sample, and compare it to a reference transient. For optically thick samples, the reference is typically a transient through air, however within this work we measure the properties of graphene, a thin conducting film supported by an optically thick substrate. In this case, one measures the THz transmission through the film on the substrate, and for a reference, measures a bare substrate identical to the one supporting the film. The following section will outline how we apply experimentally acquired and Fourier transformed THz pulses to extract information about the conductivity of graphene supported by a substrate.

3.3.1 Fresnel transmission/reflection coefficients

All samples measured within this work can be pictured with the description above, a thin conducting film supported by a thick substrate, as shown in Figure 3.5. We first consider a THz field of the form Equation 3.7 incident on the surface of a bare substrate thickness l, after passing through a slab of air of thickness δ, as depicted in Figure 3.5a.

The transmitted field will be altered depending on the thickness of the substrate (l), and its refractive index (n_s) as

$$E_{\text{sub}}(\omega) = t_{air\rightarrow sub}t_{sub\rightarrow air}E_0 e^{in_{air}\omega\delta/c}e^{n_s\omega l/c} \tag{3.8}$$

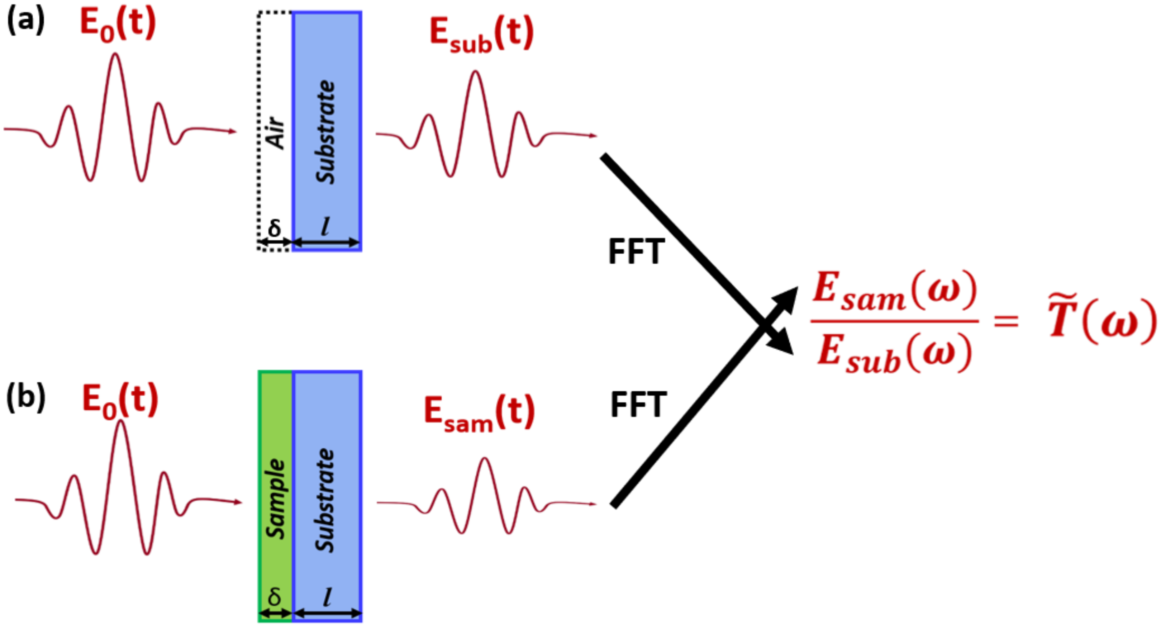

Figure 3.5: The geometry for the THz transmission of the (a) reference signal and (b) sample signal. E_0 is the incident THz field, E_{sub} is the transmitted field through the bare substrate, and E_{sam} is the transmitted field through the graphene sample and substrate.

where $t_{i\to j}$ are the Fresnel transmission coefficients from material i to material j at normal incidence. They are written as[114]

$$t_{i\to j} = \frac{2n_i}{n_i + n_j} \tag{3.9}$$

Similarly, for the transmitted field through the conducting film and substrate as shown in Fig 3.5b, we have

$$E_{\text{sam}}(\omega) = t_{air\to sam} t_{sam\to sub} t_{sub\to air} E_0 e^{in_g\omega\delta/c} e^{in_s\omega l/c} F_g \tag{3.10}$$

where n_g and δ are the refractive index and thickness of the graphene film respectively. F_g is a term[115] that accounts for the internal Fabry-Perot reflections within the graphene film. It is written as $F_g = (1 + r_{air\to sam} r_{sam\to sub} e^{2in_{sub}\omega\delta/c})^{-1}$, where r_{ij} are the Fresnel reflection coefficients. These are written as[114]

$$r_{ij} = \frac{n_i - n_j}{n_i + n_j} \tag{3.11}$$

Therefore, the transmission through the thin conducting film is written as the ratio of the two Fourier transformed fields

$$\tilde{T}(\omega) = \frac{E_{sam}(\omega)}{E_{sub}(\omega)} = \frac{t_{air\to sam}t_{sam\to sub}}{t_{air\to sub}}\left(\frac{e^{-in_{air}\omega\delta/c}e^{in_g\omega\delta/c}}{1 + r_{air\to sam}r_{sam\to sub}e^{2in_g\omega\delta/c}}\right) \tag{3.12}$$

and the Fresnel reflection and transmission coefficients can be straight-forwardly substituted using Equations (3.9) and (3.11). We can then re-write the transmission as

$$\tilde{T}(\omega) = \frac{n_g(1+n_s)e^{-i\omega\delta/c}}{n_g(1+n_s)\cos(n_g\omega\delta/c) - i((n_g)^2 + n_s)\sin(n_g\omega\delta/c)} \tag{3.13}$$

where $n_{air} = 1$. Furthermore, considering that the thickness of the film classifies as (i) 'thin' and (ii) highly conductive, we make the approximations that (i) $n\omega\delta/c \ll 1$ or $\delta \ll \lambda/n$ and (ii) $(n_g)^2 \gg n_s$. We then have for the transmission:

$$\tilde{T}(\omega) = \frac{(1+n_s)}{(1+n_s) - i(n_g^2)(\omega\delta/c)} \tag{3.14}$$

Finally, we can write the refractive index of the film as a function of the complex sheet conductivity $(\tilde{\sigma}(\omega))$[75] through Maxwell's equations,[116] where $(n_g)^2 = \epsilon_g = \frac{i\tilde{\sigma}(\omega)}{\delta\epsilon_0\omega}$ giving:

$$\tilde{T}(\omega) = \frac{1+n_s}{1+n_s+Z_0\tilde{\sigma}(\omega)}, \quad \tilde{\sigma}(\omega) = \frac{(1+\tilde{n}_{sub})}{Z_0}\left(\frac{1}{\tilde{T}(\omega)} - 1\right) \tag{3.15}$$

where $Z_0 = 1/\epsilon_0 c = 377\Omega$ is the vacuum impedance. This is known as the Tinkham equation,[117] and is certainly valid for the terahertz response of graphene which is a conducting film on the order of only a few Å thick. Therefore, the complex transmission can be written in terms of the directly transmitted THz field, resulting in the analytical expression for the complex sheet conductivity[20,118]

$$\tilde{\sigma}(\omega) = \frac{(1+\tilde{n}_{sub})}{Z_0}\left(\frac{1}{\tilde{T}(\omega)} - 1\right) \tag{3.16}$$

where $\tilde{T}(\omega) = |T(\omega)|e^{i\Delta\phi}$. Therefore, the real and complex conductivities (σ' and σ'' respectively), can be directly extracted by measuring the THz electric field through the sample+substrate, and just the bare substrate such that

$$\sigma'(\omega) = \frac{(1+\tilde{n}_{sub})}{Z_0}\left(\frac{\cos(\Delta\phi)}{|T(\omega)|} - 1\right), \quad \sigma''(\omega) = -\frac{(1+\tilde{n}_{sub})}{Z_0}\frac{\sin(\Delta\phi)}{|T(\omega)|}. \tag{3.17}$$

Chapter 4

Complex conductance of CVD graphene

4.1 Broadband conductance spectra

In this thesis we measure the oscillating THz field through graphene samples and a reference, and extract the transport properties of the films using a standard analysis and fitting procedure. More specifically, the transport properties represent four characteristics of the film, the DC conductivity (σ_{DC}), the average scattering time (τ), the carrier density/doping (N_S), and the carrier mobility (μ). This chapter will outline that procedure based on the already established understanding of how THz frequencies induce intraband transitions and probe these free carrier characteristics. Specifically, we extract properties of graphene sheets supported by technologically relevant substrates for current and potential future electronics applications. THz spectroscopy is particularly suitable to this task not only due to its ideally tuned energy for inducing the necessary transitions, but also due to the non-contact, minimally invasive nature of the optical measurement. Without the need for deposition of metal contacts or application of current, the sample can be characterized and remain useful for applications after the measurement.

4.1.1 Calculating conductance spectra

THz transmission measurements are used to extract the optical conductivity of an arbitrary graphene film deposited on a substrate, within the spectral region determined by the oscillating THz field. Within our lab, the output spectral content can range from 0.3-3 THz, to a relatively more broadband window of 0.5-6 THz. This broader spectral range is achieved with a newly demonstrated setup combining a photonic crystal fibre (PCF) with a Yb:KGW ultrafast laser, and using GaP for nonlinear generation and detection of THz radiation.[119] Some measurements presented were taken without the PCF (as it was temporarily out of service), and consequently are over a smaller THz spectral window. Importantly we note that in all measurements, the spectral content is sufficiently broad to well capture the samples scattering behaviour. In other words, the scattering rate is generally smaller than the measurable frequencies ($\Gamma < 2\pi f$). In the greater context of this work, we measure conductance spectra for graphene supported by different substrates. In this section, we will review the analysis procedure for measuring the conductance spectrum of graphene on one arbitrary substrate.

As described in Section 3.3 a reference and sample time domain waveform are collected, as pictured in Figure 4.1a. We measure 6-8 ps long scans (shown in the inset of Figure 4.1a), to ensure we capture the full THz waveform. However, 6-8 ps long scans are not always necessary in extracting physical information, and in the data processing phase we select only the region of the pulse that contains the main THz oscillations. This is called time-windowing the data. The windowed data corresponds to the gray region in the inset of Figure 4.1a. To improve the measurement accuracy and to quantify error, for a given sample or reference measurement we collect 5 to 10 transients on the same spot, and take the average of those. In Figure 4.1a, the transients shown are the average of 10 scans at the same spot on the substrate (E_{sub}) and 10 scans at the same spot on the graphene (E_{sam}). When performing measurements we take the transients through the sample and reference in pairs, such that 10 references are measured, and immediately after 10 samples are measured. This is repeated as we scan across the sample so that we are not sensitive to laser drift/fluctuations over time.

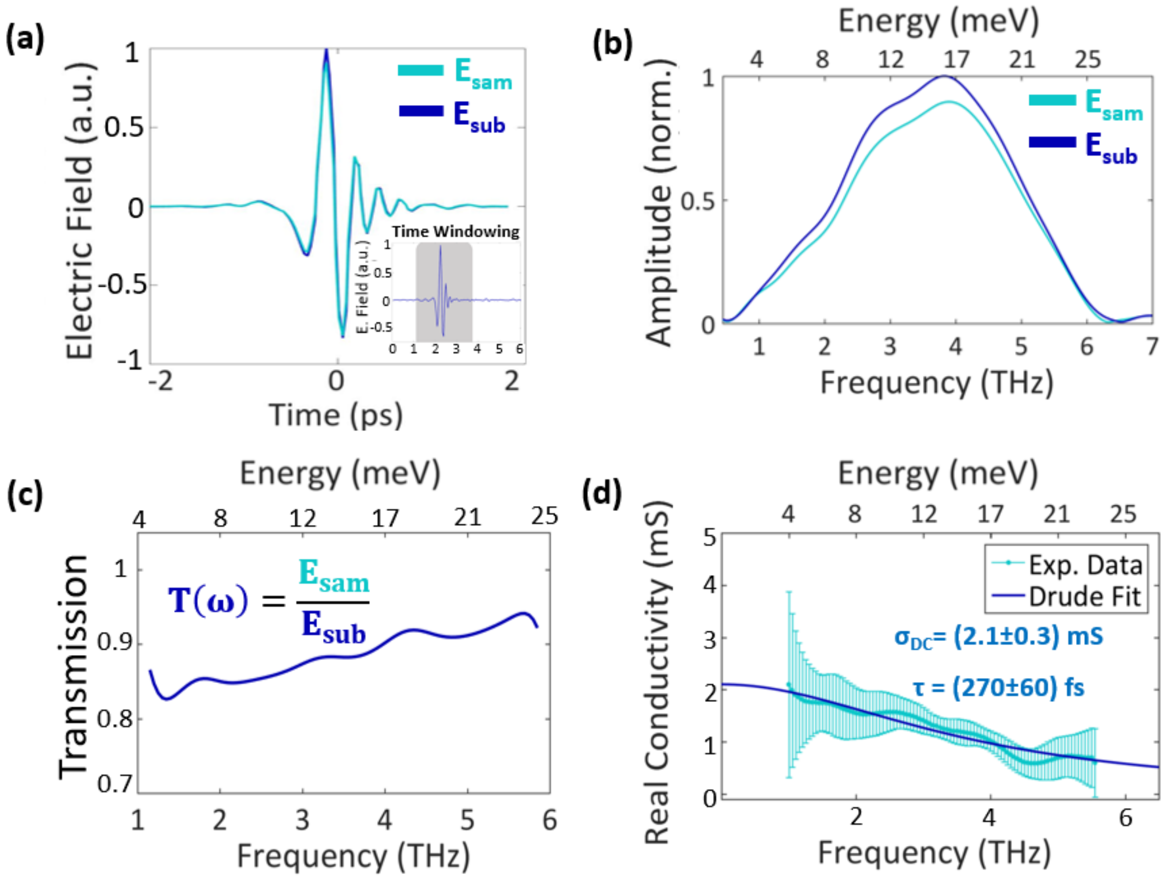

Figure 4.1: Four important steps in THz spectroscopy to extract the conductance spectrum for a graphene film supported by a substrate. (a) Reference and sample time domain wave forms are collected as raw data. Inset: 6-8 ps long scan. Grey region represents the important THz oscillations, and is the selected windowed data shown in the main figure. (b) A fast Fourier transform is performed on the two time domain wave forms in MATLAB to reveal the spectral amplitude. (c) The ratio of the sample to reference spectrum is calculated and plotted as the frequency dependent transmission (d) The corresponding conductance spectrum is calculated from (c) based on Equation (3.17). Error bar is calculated by performing many scans over the same spot, and calculating the deviation in the final conductivity. The final conductance data is then fit to the Drude model.

We then apply the FFT algorithm in MATLAB on the averaged time domain transients to retrieve the amplitude spectra as in Figure 4.1b. Taking the ratio of the transmitted pulses as outlined in Section 3.3 we measure the frequency dependent transmission as shown in Figure 4.1c. The real contribution to the conductivity ($\sigma'(\omega)$) is then directly analytically calculated based on Equation (3.17), (as shown in 4.1d). To quantify a margin of error for $\sigma'(\omega)$, we perform this analysis for every time domain transient collected at a given spot, and take the standard deviation of the conductance curves as the error bar. To obtain a representative measurement for a given sample, this analysis is repeated for several spots across the (1×1 cm) sample. The final conductance curve reported for a given sample represents the average conductance curve for all spots collected, and the error margin represents the standard deviation of all conductance curves collected across that sample. It is also important to note here that because the spot size of the THz focus is much larger than the length scales of carrier motion in graphene, one THz measurement spot is already an excellent estimator of that CVD graphene sample's average conductivity.[22]

Exclusion of the imaginary contribution

As discussed previously in this thesis, a great advantage of time-domain terahertz spectroscopy is the ability to measure the oscillating THz field, and therefore have access to the amplitude and phase information in the pulse. This makes the calculation of complex material properties straight forward, without need for the beautiful, yet complex Kramers-Kroenig integrals. Within this work, we do not apply the imaginary conductivity to the fitting procedure to extract material properties for the following reason.

Recall we measure the transmission ratio through a substrate as a reference for the measurement with a thin graphene film supported by that same substrate. The amplitude transmission ratio is pronounced, as carriers in graphene can absorb as much as $\sim$20%. The phase delay imparted to the pulse due to the atomically thick graphene is not nearly so pronounced, and is much more difficult to reliably measure. Furthermore, as seen in Equation (3.17), $\sigma''(\omega)$ is incredibly sensitive to $\Delta\phi$, as it is proportional to $\sin(\Delta\phi) \approx \Delta\phi$, for $\Delta\phi \approx 0$. While careful measurement of $\sigma''(\omega)$ is possible, and in principle would improve the reliability of the fitting, $\sigma'(\omega)$ alone has been routinely determined as sufficient to robustly extract carrier properties.[88, 120, 121]

4.1.2 Extracting optical properties from conductance spectra

The average conductance spectrum for a given sample can be fit to the real part of the Drude model as written in Equation (2.20), allowing direct extraction of σ_{DC} and τ from the Drude fit, and straight forward calculation of N_S and μ. Measurement of the average σ_{DC}, τ, N_S, and μ for large area CVD graphene films has previously been reported on by many groups using time domain terahertz spectroscopy. Table 4.1 summarizes the reported extracted parameters from the literature, sorted by their underlying substrate. We note that SiO_2 and quartz are compositionally the same, however are considered distinct substrates here. Thermally grown SiO_2 is an amorphous material, some oxygen atoms will bond to only one silicon atom. Quartz represents the SiO_2 structure in a perfect crystalline form, where all oxygen atoms bond with two silicon atoms.

	σ_{DC} **(mS)**	τ **(fs)**	N_S **($\times 10^{12}$ cm^{-2})**	μ **(cm^2/Vs)**
Silicon	1.7, 2.4[20]	380[96]	6.9[96]	2100[96]
SiO_2	0.8,[21] 2.19[122]	69, 73,[122] 351[76, 123]	1.05,[19] 4.5,[123] 5.5[122]	2208, 2467,[123] 2700[19]
Si_3N_4	1.5,[75] 3.2[88]	78[122]	6,[75] 22.5[88]	845,[88] 1352[75]
PET	3.5, 4.1[89]	68, 81[89]	Not reported	441[89]
Quartz	Not reported	124, 139,[84] 350[124]	0.6, 1.6,[84] 6[124]	2000,[124] 2350, 2940[84]

Table 4.1: Extracted properties of CVD graphene films reported in the literature.

The fitting in this thesis is performed in OriginPro, and is programmed to perform a weighted fit based on the error in the real conductivity. In the fitting algorithm data points with larger error are weighted less heavily than those with smaller error. This allows for the most accurate parameter extraction that is preferentially based on the frequency range with the strongest signal (restricting the fit from being distorted by the edge of the spectral content, where we have a smaller signal to noise ratio).

We perform this fitting procedure for graphene samples supported by seven previously described substrates, with the extracted parameters plotted in Figures 4.2, and 4.3. Each data point represents the average value on a sample across many collection points. The errorbar represents one standard deviation of the extracted property across those collection points. Extracted parameters are reproducible within the errorbar for nearly every measurement.

For our devices, we measure DC sheet conductances between 0.55 and 3 mS (as seen in Figure 4.2a). These conductivities are comparable to those discussed above from the literature. They are also consistent with other GFET devices prepared within this work that exhibit sheet resistance between 400 and 2000 Ω, measured using a two point probe electronic measurement (such as that shown in Figure 2.1.3).[125] Furthermore we measure average scattering times for samples to be between 100 and 600 fs (as seen in Figure 4.2b). These values are high compared to those commonly reported in literature, however are not surprising for clean, well transferred graphene that was grown on single crystalline copper foils.[22]

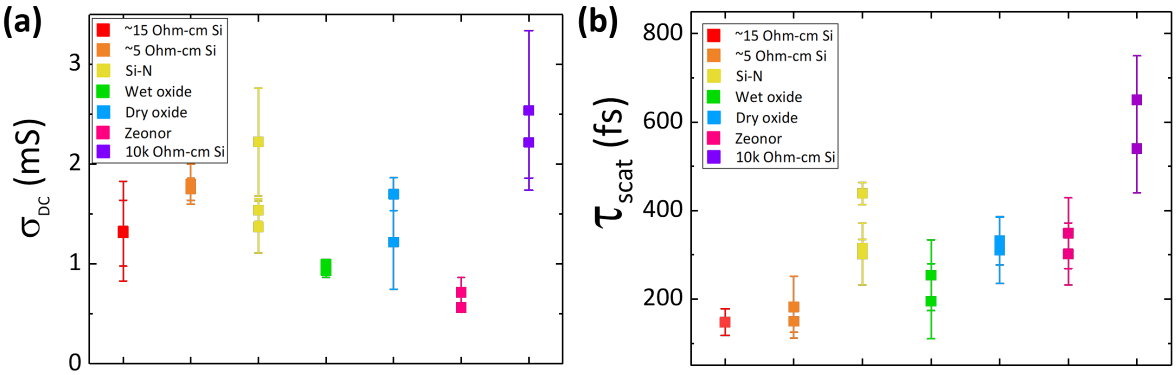

Figure 4.2: Average (a) DC conductivities and (b) scattering times for large area graphene sheets supported by 7 substrates.

Using the extracted σ_{DC} and τ, carrier density (N_S) and mobility (μ) can be directly calculated and averaged to extract a representative density and mobility for a given sample. Carrier density is calculated directly from the Drude weight, as in Equation (2.20)

$$N_S = \frac{\pi \hbar^2}{v_F^2 e^4} \left(\frac{\sigma_{DC}}{\tau} \right)^2 \tag{4.1}$$

and the carrier mobility from the well known relation

$$\mu = \frac{\sigma_{DC}}{e N_S} = \frac{v_F^2 e^3}{\pi \hbar^2} \frac{\tau^2}{\sigma_{DC}} = \frac{v_F e}{\sqrt{\pi} \hbar} \frac{\tau}{\sqrt{N_S}} \tag{4.2}$$

We measure carrier density doping levels between (0.8-9)$\times 10^{12}$ cm^{-2} (Figure 4.3a), and drift mobilities ranging from (200-6000) cm^{2}V^{-1}s^{-1} (Figure 4.3b). These values are again, in line with the above summarized literature for wet transferred CVD graphene, that becomes unintentionally doped during transfer.[22]

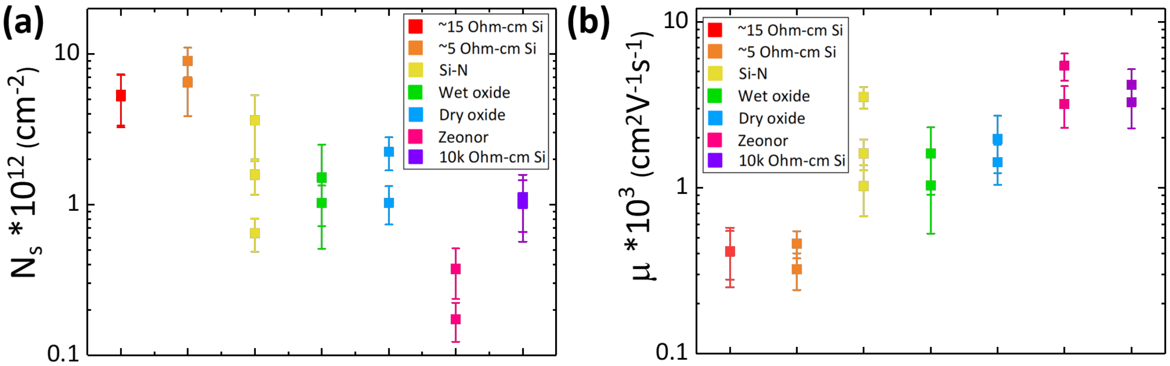

Figure 4.3: Average (a) carrier densities and (b) carrier mobilities for large area graphene sheets supported by 7 substrates.

Notably, for the device measured by backgate sweeping (in Section 2.1.3) we find the measured mobilities to agree within the range of error: μ_{BG} = 2300 cm^{2}V^{-1}s^{-1}, versus μ_{THz} = (1900 ± 600) cm^{2}V^{-1}s^{-1}. Furthermore, we find the measured carrier densities to comparatively be: N_{BG}=4.05$\times 10^{12}$cm^{-2}, versus N_{THz}=(2.06$\pm$1)$\times 10^{12}$cm^{-2}.

4.2 Environment dependent conductance properties

As can be seen in Figure 4.2 & 4.3, graphene supported by various substrates exhibits drastically different carrier properties. This is not surprising, it is well known that graphene films and their transport properties are highly susceptible to changes in environment and supporting substrate. The ultrafast transport dynamics in graphene have demonstrated sensitivity to surrounding temperature,[126] and gaseous environment,[127] and their equilibrium dynamics to the underlying substrate.[123] In Ref [123] graphene is deposited on SiO_2 substrates with four types of buffer layer (polar oxides-$SrTiO_3$/ZnO and organic polymer films-HMDS/PMMA). N_S, and μ are extracted in the FIR using Fourier Transform Infrared Spectroscopy (FTIR). They find that mobility is vastly changed for different substrates, with μ ranging from 1594 $cm^2V^{-1}s^{-1}$ on ZnO to 11680 $cm^2V^{-1}s^{-1}$ on HMDS. They argue that μ can be enhanced with the reduction of the *substrate* carrier density to minimize substrate induced charge doping. They argue that increased charged impurities in the substrate adds more scattering sources for the graphene carriers, and that a substrate with high dielectric constant (ϵ) may be preferable, as the potentials from charged impurities are screened more effectively. The substrate effect on graphene transport properties has also been studied by fabricating graphene field effect transistors[61] (GFETs), similar to those shown in Figure 2.12 and fabricated in Section 2.1.1. In Ref [61] GFETs are fabricated on several technologically relevant dielectric substrates within the semiconductor industry: SiO_2, HfO_2, Al_2O_3, Si_3N_4 and tetraethylorthosilicate (TEOS)-oxide. Carrier properties are extracted for each substrate based on the FET measurement procedure outlined in Section 2.1.3, as well as by Raman spectroscopy. They consistently find that the mobility of graphene is vastly different for the different substrates, with μ ranging from 4000 $cm^2V^{-1}s^{-1}$ on HfO_2 to 10000 $cm^2V^{-1}s^{-1}$ on SiO_2 and Si_3N_4. They ultimately attribute a higher mobility to be correlated with fewer scattering centres in the substrate. They find the mobility of graphene supported by Si_3N_4 superior to the other substrates, and to be comparable to that supported by SiO_2.

As graphene integrated electronics become an attractive pathway to improving future devices, a thorough understanding of the effect substrate has on carrier transport becomes essential, specifically for substrates that show promise in technologically relevant applications. To date there exists no systematic study that measures the transport properties of graphene supported by substrates with quantifiable differences in their density of charged impurities. The role of this work is to provide a study that measures the substrate dependent transport properties of graphene, using substrates that both are commonly used in Si-CMOS, and contain a (quasi) quantifiable density of charged impurities, and to do so using the non-contact benefits of THz spectroscopy. As mentioned, we find that graphene deposited on these varying devices indeed demonstrates vastly differing transport properties. The following section will discuss more deeply what else (aside from substrate charged impurities), can limit the carrier mobility, and therefore overall device performance in large-scale CVD graphene.

4.2.1 Limitations to device performance

The limiting factors that inhibit the transport properties of CVD graphene are primarily due to the growth and subsequent transfer procedure. The first limitation we will discuss is the prominence of grain boundaries. Grain boundaries are defined to be linear defects that are formed during the coalescence of two single crystalline graphene domains[128] (visualized in Figure 4.4a). They are a consequence of the CVD growth process that limits the mechanical strength of large area films, and act as line-shaped defects in limiting carrier transport.[22] Grain boundaries produce back scattering events (due to their linear shape)[22] that inhibit the low frequency (σ_{DC}) conductivity through a sign reversal of the current impulse response. Since carriers back scatter a net drift is not accumulated, and σ_{DC} is suppressed. Samples with small conductive domains that are dominated by this sort of back scattering must be treated within the Drude-Smith model,[122] where a back scattering term (c) accounts for the diminished conductivity at low frequencies in the Drude model.[129] In practice today, high quality CVD graphene has single crystalline domains typically several microns in diameter, with the graphene used in this work quoted to have grain size of up to 20 μm as specified by the supplier, Graphenea.

CVD graphene also suffers from residues left during the wet transfer process. Common residues that leave damage to the sample include cracks, tears, and wrinkling of the film. These sort of residues are marked in Figure 4.4b. In the samples prepared here, cracks, wrinkles, and tears are minimized through practice and optimization of the transfer technique, however they are inevitable. Typically these residues are separated by 10s of μm. Moreover, residues are left on the surface from the wet transfer technique such as PMMA. Removing PMMA residues has long been a critical problem in the optimization of graphene surface cleanliness, they are known to alter the electronic properties of graphene through p-doping, and can also act as scattering centers.[130] Acetone is used as a solvent to remove the bulk of PMMA residue, and as mentioned in Section 2.1.2, they can be further reduced by annealing samples in forming gas at 400°C. In this work the average separation between adjacent PMMA aggregates is calculated (as described in Section 2.1.3) and are found to be separated by average distances ranging between 2-15 μm.

Finally, transport properties can be influenced by gas and water molecules adsorbed at the surface, trapped between the film and the substrate, or trapped within the substrate itself.[131] These trapped molecules can create charge potentials that again inhibit the mobility by creating scattering centers.[132] While it is difficult to assess ourselves the separation between adjacent adsorbed or trapped charge potentials, the typical con-

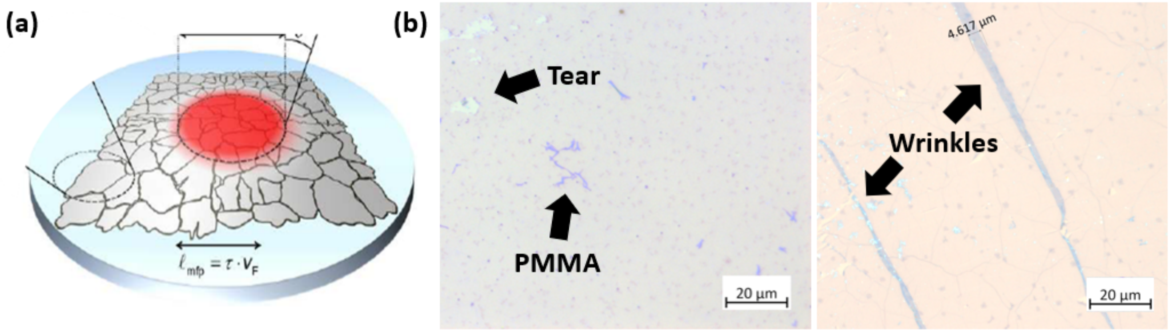

Figure 4.4: (a) Visualization of the domains separated by grain boundaries that make up the CVD graphene surface. Domains within this work are typically 10's of μm wide. Red spot represents a THz beam focus demonstrating how it probes over many grain boundaries. Reprinted from.[22] (b) Physical defects that result from the wet transfer process including tears in the lattice, PMMA macromolecules, and wrinkles.

centration of charged impurities in SiO_2 substrates is considered to be at least $5{\times}10^{11}$ cm^{-2},[133] corresponding to average separation distances of < 1 μm. To control the density of charged potentials in substrates within this work, we use silicon wafers with a known boron doping density, quoted by the manufacturer. We can then crudely estimate the average spacing between boron dopants, and therefore between charge potentials that create scattering centers. We can also consider the samples to have similar density of adsorbed gas or water molecules on the graphene surface as each sample is prepared and stored identically, and measurements are always performed in a nitrogen purged chamber held at a consistent relative humidity.

Overall, the carrier mobility in CVD graphene is widely understood to be limited by scattering mechanisms[81] described above, which for the most part can be described by charged impurity scattering[22] Randomly distributed charged impurities within a substrate lead to an electrostatic potential map with hills and valleys. When graphene is placed on such a substrate, the Fermi level varies spatially within the film, often referred to as forming electron-hole puddles.[134] The charged impurity that likely plays a dominant role in limiting device mobility will be that which is most densely populated, or having the minimal separation distance. As described above scattering by charged impurities trapped in or between the substrate and film is likely the dominant influence limiting the mobility. Therefore, we dedicate the following section to reviewing how the substrates used in this work vary in terms of density of charged impurities, and how this correlates to the extracted carrier properties.

Furthermore, carrier transport in graphene can be influenced by smaller scale effects including the Coulomb collapse. This effect was theorized, and subsequently observed, where the presence of supercharged impurities causes a strong Coulomb field and an unusual atomic collapse of carriers. In this work we study large area samples at room temperature, and probe dynamics averaged over hundreds of microns. Therefore, these small scale effects are not taken into account, but however remain useful to mention.

Furthermore, carrier transport in graphene can be influenced by smaller lengthscale effects including the Coulomb collapse. This effect was theorized,[135] and subsequently observed[136] where the presence of charged impurities causes a strong Coulomb field and an unusual atomic collapse of carriers. In this work we expect such effects to be negligible, as we study large area samples at room temperature, and probe dynamics averaged over hundreds of microns.

4.2.2 Substrate dependent properties of CVD graphene

To compare the difference in carrier transport of devices supported by distinct substrates, we classify samples as belonging to one of three groups based on their inferred density of charged impurities, and the bulk resistivity of the substrate:

(i) **Doped silicon** which comprise wafers with a high concentration of injected boron impurities to facilitate conduction. Boron impurities in the substrate likely form charge potentials which facilitate scattering.

(ii) **Dielectric films** grown on top of a silicon substrate are known to contain a significant amount of trapped charges due to the amorphous growth of the film that leaves dangling bonds at the silicon interface. These trapped charge centers could facilitate scattering.

(iii) **High purity** substrates, meaning that they do not contain a significant amount of trapped charges (such as those in dielectric films) or intentionally injected dopants (such as those in doped silicon). The ZEONEX substrate has high resistivity, meaning it is intrinsically a good insulator, and therefore does not necessarily contain mobile charges that could act as scattering potentials. The 10,000 Ω-cm silicon substrate contains the minimally possible amount of doping impurities, again representing highly pure silicon.

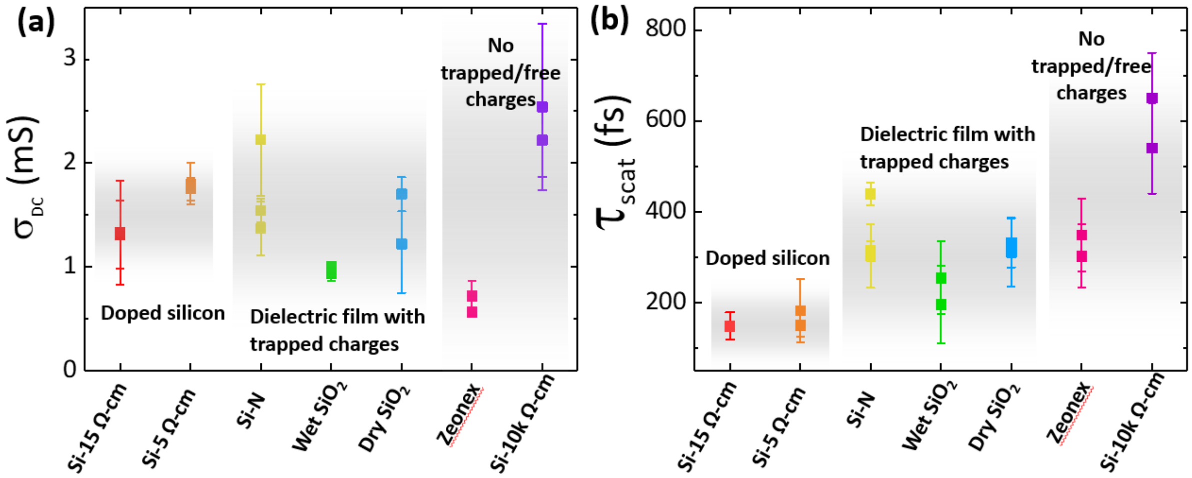

Figure 4.5: Substrate charge impurity density categorized transport properties (a) DC conductance (b) Average scattering time. Error bars represent one standard deviation for the extracted parameter taken from several scans taken across one sample.

Transport properties of the samples sorted by this substrate classification are visualized in Figure 4.5. When sorting the sample properties in this manner the following observations become apparent:

a) From Figure 4.5a, the low frequency or DC conductivity does not exhibit an obvious correlation to inferred density of charged impurities in the substrate. The DC conductivity represents the motion of carriers in the limit of an optical disturbance without a frequency dependence. It describes the **net** drift of carriers in one direction over an oscillation of one THz pulse.

Aside from correlating σ_{DC} to substrate charged impurity density, we note that the non-zero nature of σ_{DC} itself further proves that the conductive domains in our samples are larger than the mean free path of carriers. Carriers scatter several times during a THz oscillation such that they are subject to a net drift in the direction throughout the duration of the electric field, and do not undergo back scattering events that would diminish the low frequency conductivity. Furthermore, we note that the uncertainty on the DC conductance is quite different for different samples. For example the error on Wet SiO_2 is much smaller than that on pure silicon. This is attributed to differing anisotropy in the sample.

b) From Figure 4.5b, the average scattering time is smallest for graphene on boron-doped silicon, is slightly increased for graphene on a dielectric films, and is the largest for graphene on the highly pure silicon. This insinuates that the average time before a scattering event occurs is increased for the samples with less charged impurity centers because on average carriers can move further distance without experiencing a scattering potential (assuming they all move the same speed, the Fermi velocity v_F). The graphene supported by the highly resistive ZEONEX® is an outlier in this trend, as τ is comparable to dielectric film substrates.

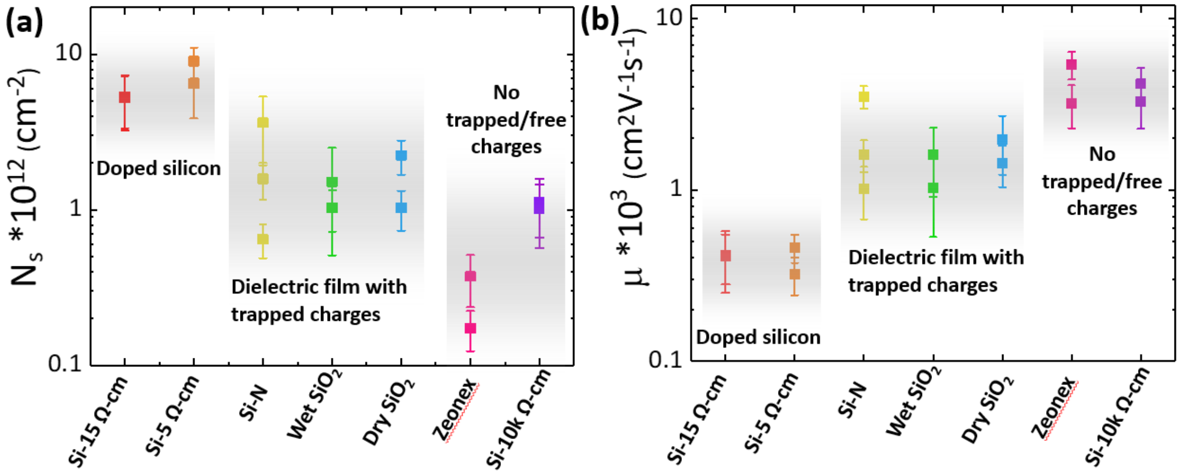

Figure 4.6: Substrate charge impurity density categorized transport properties (a) Doping/carrier density and (b) Carrier mobility. Error bars represent one standard deviation for the extracted parameter measured several times across one sample.

c) From Figure 4.6a, the doping density of the graphene lattice is generally larger for substrates with higher doping density. This is consistent with a picture in which the substrate dopes the graphene film through substrate induced charge doping. Notably, the doping density of graphene on pure silicon is larger than that of graphene on ZEONEX®, even though they are both considered here to have a high resistivity and low substrate-charge doping density. This could be due to the increased screening ability of silicon (which has a comparatively high dielectric(κ) constant compared to ZEONEX®).

d) Finally, from Figure 4.6b the mobility of graphene devices generally increases with decreased density of charged impurities in the substrate. This is consistent with a picture in which more substrate charged impurities create more scattering potentials that inhibit carrier transport and limit the mobility of graphene films. We find that for graphene supported by the highly pure silicon and flexible polymer the mobility is over an order of magnitude superior than that for graphene on doped silicon, indicating that the prominent presence of boron impurities immediately influences the resultant mobility. Furthermore, we find the mobility of graphene on these low charge density substrates to be superior to those deposited on thin dielectrics (a common substrate for graphene electronics applications due to their gating ability). This finding could be an important result for industries looking to incorporate graphene into electronics. Choice of substrate, doping level, and charged impurity concentration will limit the overall enhancement that graphene can offer in terms of improved carrier mobility in a device. Furthermore, it may elucidate that large area graphene films are more suitable for silicon electronics applications that do not require use of gate dielectrics.

Dependence of the substrate dielectric constant

It has been suggested that graphene mobility may be enhanced by using substrates with a higher dielectric constant (κ).[133] It is argued that a substrate with larger κ will more readily screen charged potentials created by trapped scattering centers, and therefore enhance the carrier mobility.[137] This effect has been investigated by several groups that typically fabricate GFET devices either supported by different dielectric gate materials,[61,138] submersed in different solvent overlayers,[139] or with different atomic layer deposited (ALD) overlayers.[137]

In Ref [61], they did not find the mobility of graphene to be enhanced for high κ substrates; device performance on SiO_2 ($\kappa = 3.9$) and Si_3N_4 ($\kappa = 7.5$) were superior to that on Al_2O_3 ($\kappa = 9$) and HfO_2 ($\kappa = 22$). In Ref [138] GFET devices are submersed in glycerol ($\kappa = 42$) and in ethanol ($\kappa = 25$). They find that the mobility is enhanced in a higher κ environment, as expected, for devices with lower mobility ($\mu <$10,000 cm^{-2}V^{-1}s^{-1}). Furthermore, they find that it is not increased by the theoretically expected amount[133] for devices with high mobility ($\mu \geq$ 10,000 cm^{-2}V^{-1}s^{-1}). From this they conclude that for the *low mobility devices* scattering is likely limited by charged impurities, as the improved dielectric media helps screen those potentials, and that for *higher mobility* devices there are likely other long range scattering mechanisms such as resonant scatterers with energy close to the Dirac point,[140] or flexural phonons (ripples)[141] limiting the mobility. Similar findings are reported in,[139] who also submersed GFET devices in media ranging in κ = 1-200, and find improved mobility performance (a few orders of magnitude) for graphene in high κ environments.

In Figure 4.7, we plot the extracted properties of samples prepared in this work as a function of the substrate dielectric constant to see if the dielectric screening effects described are consistent with mobility enhancement claims made by the above mentioned references. From Figure 4.7a & 4.7b, σ_{DC} and τ of the graphene generally increase with increased substrate κ. This could be due to the ability of the substrate to screen the charged impurities and inhibit scattering events. The exception in both of these cases however, is for graphene deposited on doped silicon.

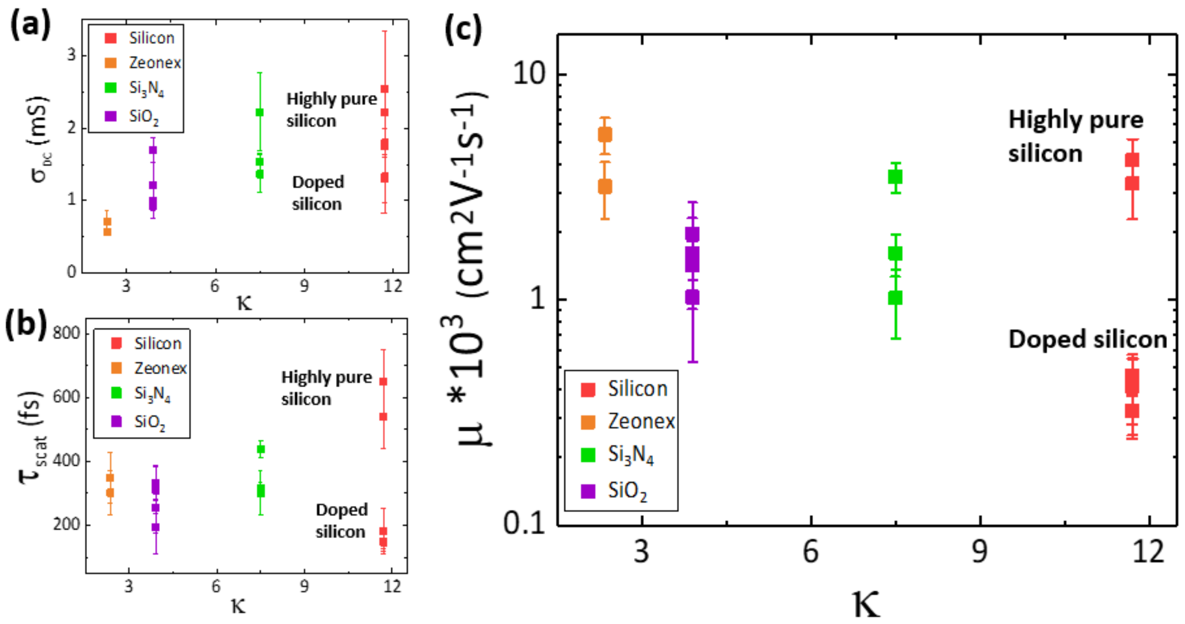

Figure 4.7: Extracted transport properties of graphene samples characterized by THz spectroscopy as a function of the substrate dielectric constant, or screening ability. (a) DC conductivity, or net charge transport (b) Average scattering time (c) Carrier doping density (d) Carrier mobility

From Figure 4.7c, it may be inferred that the carrier mobility of graphene films supported by substrates with increased κ is improved, with some important observations. The improvement is not remarkable, and is not truly distinguishable within the measurement error. Therefore, we cannot conclude within this work that a sample with higher dielectric constant results in an improved carrier mobility. Furthermore, graphene on ZEONEX®, demonstrates a high mobility, even though it has the smallest dielectric constant. This would indicate that the screening by the substrate of charged impurities is not contributing to the high mobility, and that the limiting factor for transport in this device may not be related to charged impurity scattering, but limited by an effect that is not currently taken into account. This could include the substrate roughness, the manner in which graphene conforms to the substrate, or the tendency for the substrate to trap water or air molecules at the film/substrate interface. We could infer that a graphene films that is smoother would exhibit a higher mobility. We could also infer that graphene on a hydrophobic substrate could have less water molecules trapped at the interface, and therefore less charged impurities to act as scatterers. Also from Figure 4.7c, the mobility of graphene deposited on doped silicon is remarkably small, regardless of silicons comparatively strong ability to screen charged impurities. In this case, we could conclude that injected boron dopants are too prevalent for silicon to effectively screen, and improve the device mobility. Within this discussion, it is important to note that the effect of how substrate dielectric constant plays a role in affecting the mobility of graphene is currently under debate[138, 139, 142]

Chapter 5

Conclusion and Outlook

In this work we demonstrate the implementation of terahertz transmission spectroscopy for probing the equilibrium carrier dynamics of monolayer CVD graphene samples supported by seven substrates. We describe a repeatable process for fabricating custom size large area graphene samples, and briefly review some techniques for metrologically characterizing their physical properties including residues, thickness, and lattice defects. We present the workings behind time domain terahertz spectroscopy, and outline how one can experimentally extract conductance properties using transmission measurements. We find that the resulting conductance of the graphene films indeed suits a Drude model framework for understanding the carrier dynamics, consistent with others in the field. Furthermore, our results demonstrate how the resulting transport properties vary depending on the choice of substrate. We find that for substrates with an increased density of charged impurity scattering centers, graphene films exhibit lower carrier mobility. We find that graphene deposited on substrates with lower charged impurity densities, including ultra-pure silicon and a resistive polymer demonstrate a higher mobility than commonly used gating substrates (SiO_2 and Si_3N_4), indicating that graphene may be best suited for integration into silicon electronics applications, and non-gating technologies. Finally, we find that for samples supported by substrates with higher dielectric constant that the resulting mobility could be inferred to be improved, with exceptions. Graphene on silicon with high doping density demonstrates a low mobility, regardless of silicons high dielectric constant. Furthermore, graphene on ZEONEX demonstrates a high mobility, despite its low dielectric constant. This suggests that the effect of substrate screening may help improve the mobility, but that there could be a different effect not currently taken into account that supports the high mobility in the graphene-ZEONEX device.

Future Work

The work presented in this thesis represents a study of the equilibrium carrier dynamics in graphene. Naturally, the next steps in this project could be to use the pump pulse line to excite carriers in graphene at a tuned time delay to a THz probe line. This is called optical pump-terahertz probe (OPTP) and could allow us to study the picosecond time dependent dynamics of photoexcited carriers. We could monitor the change in photoconductivity due to carrier injection across our accessible THz frequency bandwidth, and compare the results on the distinct substrates applied here. This could allow us to have better understanding of the scattering dynamics, through observation of either enhanced or suppressed frequency dependent conductivity.

Chapter 6

Appendices

6.1 Library of conductance spectra

Within this appendix are the raw conductivity spectrum data used to fit to the Drude model. These spectra represent the real part of the conductivity, calculated using Equation 3.17, and the raw transmission data. Each spectrum presented represents the average conductivity taken over many spots on a sample, measured on a given day. The spectra included the fitted parameters using the OriginPro weighted fit, that being σ_{DC} and τ. They also contain the directly calculated parameters N_S, and μ. The errors associated with each parameter represent one standard deviation of that parameter measured across many spots on the same sample. Finally, in several spectra there are oscillations within the raw conductivity data. These oscillations are not intrinsic to the material optical response, and are due to either laser fluctuations or reflections within the substrate. Because we extract an error on the conductance by measuring repeated transients, the oscillations become increasingly washed out, and the Drude fit generally falls within the measurement error.

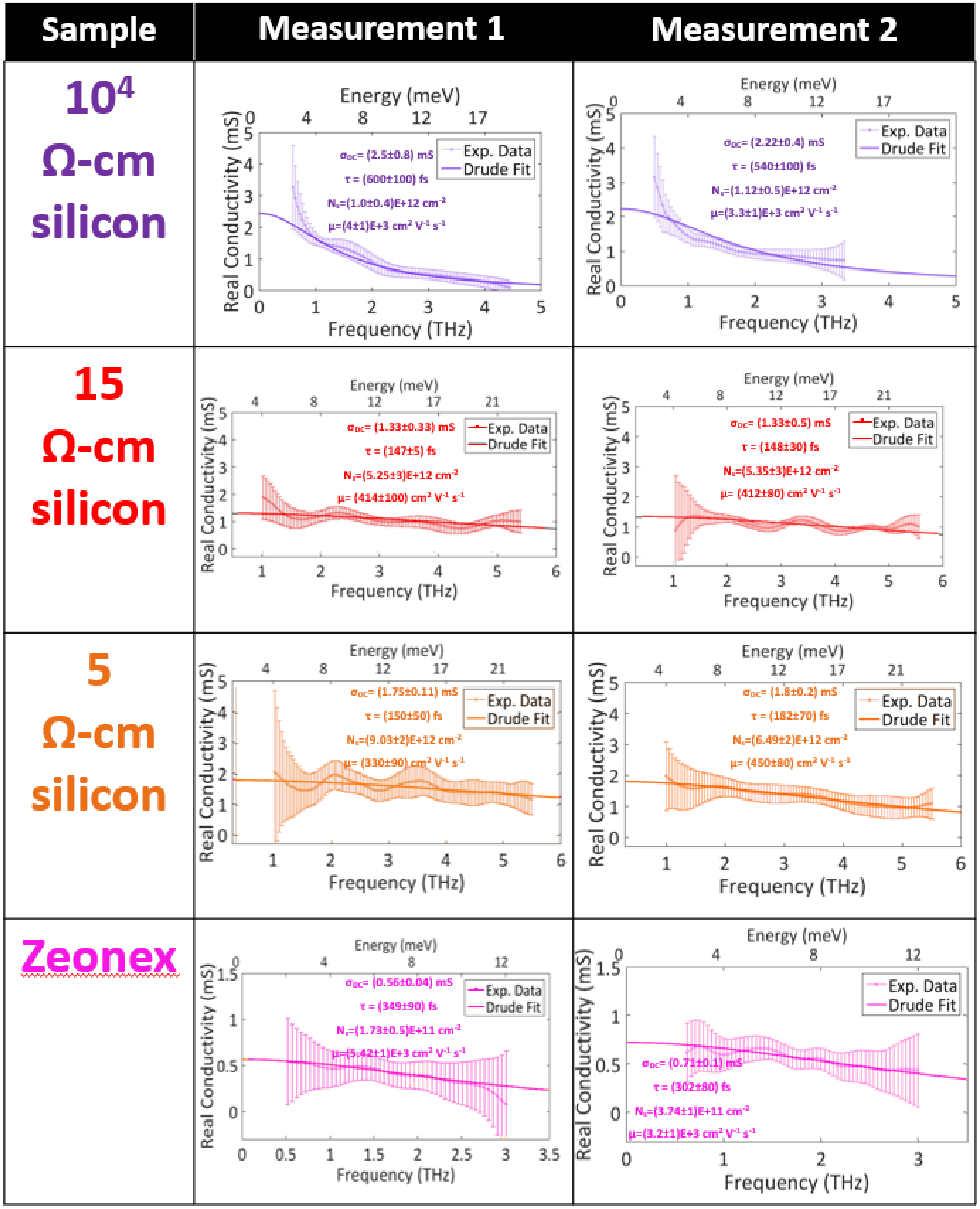

Figure 6.1: This figure summarizes and organizes the average conductance spectra measured across a sample on a given measurement day. It includes all conductance data and extracted Drude fit parameters for graphene samples supported by all studied substrates.

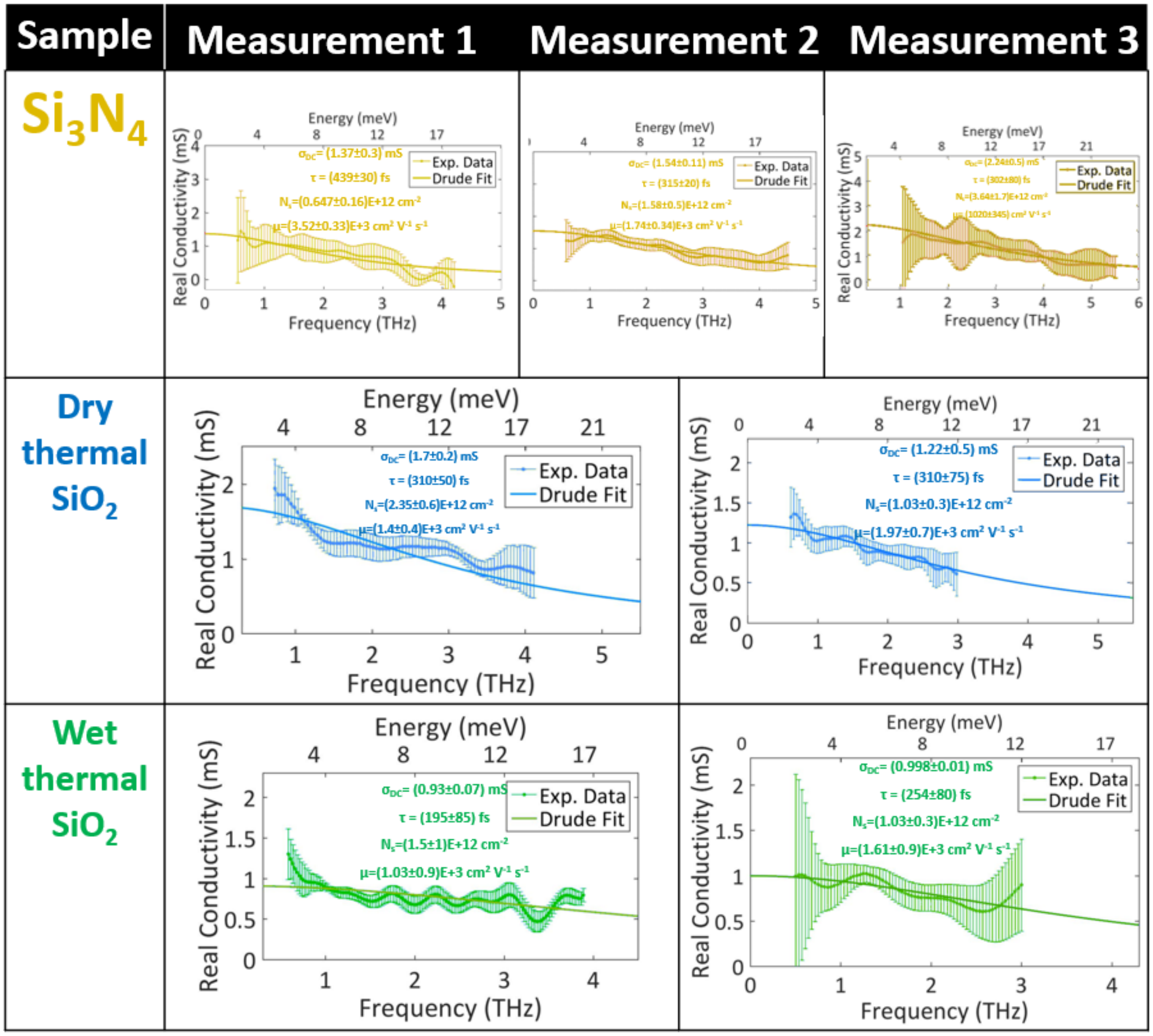

Figure 6.2: This figure summarizes and organizes the average conductance spectra measured across a sample on a given measurement day. It includes all conductance data and extracted Drude fit parameters for graphene samples supported by all studied substrates.

Bibliography

[1] Pulickel Ajayan, Philip Kim, and Kaustav Banerjee. van der waals materials. *Physics Today*, 69:9–38, 2016.

[2] Fengnian Xia, Han Wang, Di Xiao, Madan Dubey, and Ashwin Ramasubramaniam. Two-dimensional material nanophotonics. *Nature Photonics*, 8(12):899, 2014.

[3] Claire Ashworth. 2d materials: the thick and the thin. *Nature Reviews Materials*, 3(4):1–1, 2018.

[4] Kostya S Novoselov, Andre K Geim, Sergei V Morozov, D Jiang, Y_ Zhang, Sergey V Dubonos, Irina V Grigorieva, and Alexandr A Firsov. Electric field effect in atomically thin carbon films. *science*, 306(5696):666–669, 2004.

[5] P. R. Wallace. The band theory of graphite. *Phys. Rev.*, 71:622–634, May 1947.

[6] Andre K Geim and Irina V Grigorieva. Van der waals heterostructures. *Nature*, 499(7459):419–425, 2013.

[7] Frank Schwierz, Jörg Pezoldt, and Ralf Granzner. Two-dimensional materials and their prospects in transistor electronics. *Nanoscale*, 7(18):8261–8283, 2015.

[8] Deji Akinwande, Cedric Huyghebaert, Ching-Hua Wang, Martha I Serna, Stijn Goossens, Lain-Jong Li, H-S Philip Wong, and Frank HL Koppens. Graphene and two-dimensional materials for silicon technology. *Nature*, 573(7775):507–518, 2019.

[9] Sujay B Desai, Surabhi R Madhvapathy, Angada B Sachid, Juan Pablo Llinas, Qingxiao Wang, Geun Ho Ahn, Gregory Pitner, Moon J Kim, Jeffrey Bokor, Chenming Hu,

et al. Mos2 transistors with 1-nanometer gate lengths. *Science*, 354(6308):99–102, 2016.

[10] FHL Koppens, T Mueller, Ph Avouris, AC Ferrari, MS Vitiello, and M Polini. Photodetectors based on graphene, other two-dimensional materials and hybrid systems. *Nature nanotechnology*, 9(10):780, 2014.

[11] Stijn Goossens, Gabriele Navickaite, Carles Monasterio, Shuchi Gupta, Juan José Piqueras, Raúl Pérez, Gregory Burwell, Ivan Nikitskiy, Tania Lasanta, Teresa Galán, et al. Broadband image sensor array based on graphene–cmos integration. *Nature Photonics*, 11(6):366–371, 2017.

[12] Tobias Rauch, Michaela Böberl, Sandro F Tedde, Jens Fürst, Maksym V Kovalenko, Günter Hesser, Uli Lemmer, Wolfgang Heiss, and Oliver Hayden. Near-infrared imaging with quantum-dot-sensitized organic photodiodes. *Nature Photonics*, 3(6):332, 2009.

[13] Fazel Yavari and Nikhil Koratkar. Graphene-based chemical sensors. *The journal of physical chemistry letters*, 3(13):1746–1753, 2012.

[14] Ranjana Rautela, Samantha Scarfe, Jean-Michel Guay, Petr Lazar, Martin Pykal, Saied Azimi, Cedric Grenapin, Justin Boddison-Chouinard, Alexei Halpin, Weixiang Wang, Lukasz Andrzejewski, Ryan Plumadore, Jeongwon Park, Jean-Michel Menard, Michal Otyepka, and Adina Luican-Mayer. Mechanistic insight into the limiting factors of graphene-based environmental sensors. *ACS Applied Materials & Interfaces*, 11(9):764–767, 2020.

[15] Fredrik Schedin, Andrei Konstantinovich Geim, Sergei Vladimirovich Morozov, EW Hill, Peter Blake, MI Katsnelson, and Kostya Sergeevich Novoselov. Detection

of individual gas molecules adsorbed on graphene. *Nature materials*, 6(9):652–655, 2007.

[16] CW Chen, SC Hung, MD Yang, CW Yeh, CH Wu, GC Chi, FPSJ Ren, and SJ Pearton. Oxygen sensors made by monolayer graphene under room temperature. *Applied Physics Letters*, 99(24):243502, 2011.

[17] Eric Singh, M Meyyappan, and Hari Singh Nalwa. Flexible graphene-based wearable gas and chemical sensors. *ACS applied materials & interfaces*, 9(40):34544–34586, 2017.

[18] Jibo Zhang, Rongguo Song, Xin Zhao, Ran Fang, Bin Zhang, Wei Qian, Jingwei Zhang, Chengguo Liu, and Daping He. Flexible graphene-assembled film-based antenna for wireless wearable sensor with miniaturized size and high sensitivity. *ACS Omega*, 2020.

[19] Jason Horng, Chi-Fan Chen, Baisong Geng, Caglar Girit, Yuanbo Zhang, Zhao Hao, Hans A Bechtel, Michael Martin, Alex Zettl, Michael F Crommie, et al. Drude conductivity of dirac fermions in graphene. *Physical Review B*, 83(16):165113, 2011.

[20] JL Tomaino, AD Jameson, JW Kevek, MJ Paul, AM Van Der Zande, RA Barton, PL McEuen, ED Minot, and Yun-Shik Lee. Terahertz imaging and spectroscopy of large-area single-layer graphene. *Optics express*, 19(1):141–146, 2011.

[21] Jonas D Buron, Dirch H Petersen, Peter Bøggild, David G Cooke, Michael Hilke, Jie Sun, Eric Whiteway, Peter F Nielsen, Ole Hansen, August Yurgens, et al. Graphene conductance uniformity mapping. *Nano letters*, 12(10):5074–5081, 2012.

[22] Peter Bøggild, David MA Mackenzie, Patrick R Whelan, Dirch H Petersen, Jonas Due Buron, Amaia Zurutuza, John Gallop, Ling Hao, and Peter U Jepsen. Mapping the electrical properties of large-area graphene. *2D Materials*, 4(4):042003, 2017.

[23] N.W. Ashcroft and N.D. Mermin. *Solid State Physics*. Cengage Learning, 2011.

[24] AH Castro Neto, Francisco Guinea, Nuno MR Peres, Kostya S Novoselov, and Andre K Geim. The electronic properties of graphene. *Reviews of modern physics*, 81(1):109, 2009.

[25] G Dresselhaus, Saito Riichiro, et al. *Physical properties of nanotubes*. World scientific, 1998.

[26] Matthew Mecklenburg and BC Regan. Spin and the honeycomb lattice: lessons from graphene. *Physical Review Letters*, 106(11):116803, 2011.

[27] CWJ Beenakker. Colloquium: Andreev reflection and klein tunneling in graphene. *Reviews of Modern Physics*, 80(4):1337, 2008.

[28] S Das Sarma, Shaffique Adam, EH Hwang, and Enrico Rossi. Electronic transport in two-dimensional graphene. *Reviews of modern physics*, 83(2):407, 2011.

[29] Andre K Geim and Konstantin S Novoselov. The rise of graphene. pages 11–19, 2010.

[30] Kostya S Novoselov, Andre K Geim, Sergei Vladimirovich Morozov, Da Jiang, Michail I Katsnelson, IVa Grigorieva, SVb Dubonos, Firsov, and AA. Two-dimensional gas of massless dirac fermions in graphene. *nature*, 438(7065):197–200, 2005.

[31] MI Katsnelson, KS Novoselov, and AK Geim. Chiral tunnelling and the klein paradox in graphene. *Nature physics*, 2(9):620–625, 2006.

[32] Yuanbo Zhang, Yan-Wen Tan, Horst L Stormer, and Philip Kim. Experimental observation of the quantum hall effect and berry's phase in graphene. *nature*, 438(7065):201–204, 2005.

[33] SV Morozov, KS Novoselov, MI Katsnelson, F Schedin, DC Elias, John A Jaszczak, and AK Geim. Giant intrinsic carrier mobilities in graphene and its bilayer. *Physical review letters*, 100(1):016602, 2008.

[34] DC Elias, RV Gorbachev, AS Mayorov, SV Morozov, AA Zhukov, P Blake, LA Ponomarenko, IV Grigorieva, KS Novoselov, F Guinea, et al. Dirac cones reshaped by interaction effects in suspended graphene. *Nature Physics*, 7(9):701–704, 2011.

[35] Alexander S Mayorov, Roman V Gorbachev, Sergey V Morozov, Liam Britnell, Rashid Jalil, Leonid A Ponomarenko, Peter Blake, Kostya S Novoselov, Kenji Watanabe, Takashi Taniguchi, et al. Micrometer-scale ballistic transport in encapsulated graphene at room temperature. *Nano letters*, 11(6):2396–2399, 2011.

[36] Phillip N First, Walt A de Heer, Thomas Seyller, Claire Berger, Joseph A Stroscio, and Jeong-Sun Moon. Epitaxial graphenes on silicon carbide. *MRS bulletin*, 35(4):296–305, 2010.

[37] Xuesong Li, Weiwei Cai, Jinho An, Seyoung Kim, Junghyo Nah, Dongxing Yang, Richard Piner, Aruna Velamakanni, Inhwa Jung, Emanuel Tutuc, et al. Large-area synthesis of high-quality and uniform graphene films on copper foils. *science*, 324(5932):1312–1314, 2009.

[38] P Blake, EW Hill, AH Castro Neto, KS Novoselov, D Jiang, R Yang, TJ Booth, and AK Geim. Making graphene visible. *Applied physics letters*, 91(6):063124, 2007.

[39] Justin Boddison-Chouinard, Ryan Plumadore, and Adina Luican-Mayer. Fabricating van der waals heterostructures with precise rotational alignment. *JoVE (Journal of Visualized Experiments)*, (149):e59727, 2019.

[40] Keun Soo Kim, Yue Zhao, Houk Jang, Sang Yoon Lee, Jong Min Kim, Kwang S Kim, Jong-Hyun Ahn, Philip Kim, Jae-Young Choi, and Byung Hee Hong. Large-

scale pattern growth of graphene films for stretchable transparent electrodes. *nature*, 457(7230):706–710, 2009.

[41] Sukang Bae, Hyeongkeun Kim, Youngbin Lee, Xiangfan Xu, Jae-Sung Park, Yi Zheng, Jayakumar Balakrishnan, Tian Lei, Hye Ri Kim, Young Il Song, et al. Roll-to-roll production of 30-inch graphene films for transparent electrodes. *Nature nanotechnology*, 5(8):574, 2010.

[42] Domenico De Fazio, David G Purdie, Anna K Ott, Philipp Braeuninger-Weimer, Timofiy Khodkov, Stijn Goossens, Takashi Taniguchi, Kenji Watanabe, Patrizia Livreri, Frank HL Koppens, et al. High-mobility, wet-transferred graphene grown by chemical vapor deposition. *ACS nano*, 13(8):8926–8935, 2019.

[43] Xuelei Liang, Brent A Sperling, Irene Calizo, Guangjun Cheng, Christina Ann Hacker, Qin Zhang, Yaw Obeng, Kai Yan, Hailin Peng, Qiliang Li, et al. Toward clean and crackless transfer of graphene. *ACS nano*, 5(11):9144–9153, 2011.

[44] Xuesong Li, Yanwu Zhu, Weiwei Cai, Mark Borysiak, Boyang Han, David Chen, Richard D Piner, Luigi Colombo, and Rodney S Ruoff. Transfer of large-area graphene films for high-performance transparent conductive electrodes. *Nano letters*, 9(12):4359–4363, 2009.

[45] Guohui Zhang, Aleix G. Guell, Paul M. Kirkman, Robert A. Lazenby, Thomas S. Miller, and Patrick R. Unwin. Versatile polymer-free graphene transfer method and applications. *ACS Applied Materials & Interfaces*, 8(12):8008–8016, 2016. PMID: 26953499.

[46] Ji Won Suk, Alexander Kitt, Carl W Magnuson, Yufeng Hao, Samir Ahmed, Jinho An, Anna K Swan, Bennett B Goldberg, and Rodney S Ruoff. Transfer of cvd-grown monolayer graphene onto arbitrary substrates. *ACS nano*, 5(9):6916–6924, 2011.

[47] M Wang, Eui-Hyeok Yang, R Vajtai, J Kono, and PM Ajayan. Effects of etchants in the transfer of chemical vapor deposited graphene. *Journal of Applied Physics*, 123(19):195103, 2018.

[48] Jaeyeong Lee, Shinyoung Lee, and Hak Ki Yu. Contamination-free graphene transfer from cu-foil and cu-thin-film/sapphire. *Coatings*, 7(12):218, 2017.

[49] V Sorianello, M Midrio, G Contestabile, I Asselberghs, J Van Campenhout, C Huyghebaert, I Goykhman, AK Ott, AC Ferrari, and M Romagnoli. Graphene–silicon phase modulators with gigahertz bandwidth. *Nature Photonics*, 12(1):40–44, 2018.

[50] Ming Liu, Xiaobo Yin, Erick Ulin-Avila, Baisong Geng, Thomas Zentgraf, Long Ju, Feng Wang, and Xiang Zhang. A graphene-based broadband optical modulator. *Nature*, 474(7349):64–67, 2011.

[51] Christopher T Phare, Yoon-Ho Daniel Lee, Jaime Cardenas, and Michal Lipson. Graphene electro-optic modulator with 30 ghz bandwidth. *Nature Photonics*, 9(8):511–514, 2015.

[52] Ilya Goykhman, Ugo Sassi, Boris Desiatov, Noa Mazurski, Silvia Milana, Domenico de Fazio, Anna Eiden, Jacob Khurgin, Joseph Shappir, Uriel Levy, et al. On-chip integrated, silicon–graphene plasmonic schottky photodetector with high responsivity and avalanche photogain. *Nano letters*, 16(5):3005–3013, 2016.

[53] Guido Masetti, Maurizio Severi, and Sandro Solmi. Modeling of carrier mobility against carrier concentration in arsenic-, phosphorus-, and boron-doped silicon. *IEEE Transactions on electron devices*, 30(7):764–769, 1983.

[54] Houk Jang, Yong Ju Park, Xiang Chen, Tanmoy Das, Min-Seok Kim, and Jong-Hyun Ahn. Graphene-based flexible and stretchable electronics. *Advanced Materials*, 28(22):4184–4202, 2016.

[55] Beom Joon Kim, Houk Jang, Seoung-Ki Lee, Byung Hee Hong, Jong-Hyun Ahn, and Jeong Ho Cho. High-performance flexible graphene field effect transistors with ion gel gate dielectrics. *Nano letters*, 10(9):3464–3466, 2010.

[56] Nicholas Petrone, Inanc Meric, James Hone, and Kenneth L Shepard. Graphene field-effect transistors with gigahertz-frequency power gain on flexible substrates. *Nano letters*, 13(1):121–125, 2013.

[57] Jongho Lee, Li Tao, Kristen N Parrish, Yufeng Hao, Rodney S Ruoff, and Deji Akinwande. Multi-finger flexible graphene field effect transistors with high bendability. *Applied Physics Letters*, 101(25):252109, 2012.

[58] Pedro S Nunes, Pelle D Ohlsson, Olga Ordeig, and Jörg P Kutter. Cyclic olefin polymers: emerging materials for lab-on-a-chip applications. *Microfluidics and nanofluidics*, 9(2-3):145–161, 2010.

[59] E Kooi and A Schmitz. Brief notes on the history of gate dielectrics in mos devices. In *High Dielectric Constant Materials*, pages 33–44. Springer, 2005.

[60] Ming Yang, Chun Zhang, Shijie Wang, Yuanping Feng, and Ariando. Graphene on β-si3n4: An ideal system for graphene-based electronics. *AIP Advances*, 1(3):032111, 2011.

[61] Zhaoying Hu, Dhiraj Prasad Sinha, Ji Ung Lee, and Michael Liehr. Substrate dielectric effects on graphene field effect transistors. *Journal of Applied Physics*, 115(19):194507, 2014.

[62] SJ Haigh, A Gholinia, R Jalil, S Romani, L Britnell, DC Elias, KS Novoselov, LA Ponomarenko, AK Geim, and R Gorbachev. Cross-sectional imaging of individual layers and buried interfaces of graphene-based heterostructures and superlattices. *Nature materials*, 11(9):764–767, 2012.

[63] Masa Ishigami, JH Chen, WG Cullen, MS Fuhrer, and ED Williams. Atomic structure of graphene on sio2. *Nano letters*, 7(6):1643–1648, 2007.

[64] Justin Boddison-Chouinard, Samantha Scarfe, K Watanabe, T Taniguchi, and Adina Luican-Mayer. Flattening van der waals heterostructure interfaces by local thermal treatment. *Applied Physics Letters*, 115(23):231603, 2019.

[65] Daniel A. Sanchez, Zhaohe Dai, Peng Wang, Arturo Cantu-Chavez, Christopher J. Brennan, Rui Huang, and Nanshu Lu. Mechanics of spontaneously formed nanoblisters trapped by transferred 2d crystals. *Proceedings of the National Academy of Sciences*, 115(31):7884–7889, 2018.

[66] Andrea C Ferrari, JC Meyer, Vittorio Scardaci, Cinzia Casiraghi, Michele Lazzeri, Francesco Mauri, Stefano Piscanec, Da Jiang, KS Novoselov, S Roth, et al. Raman spectrum of graphene and graphene layers. *Physical review letters*, 97(18):187401, 2006.

[67] Axel Eckmann, Alexandre Felten, Artem Mishchenko, Liam Britnell, Ralph Krupke, Kostya S Novoselov, and Cinzia Casiraghi. Probing the nature of defects in graphene by raman spectroscopy. *Nano letters*, 12(8):3925–3930, 2012.

[68] Zhen Hua Ni, Ting Yu, Yun Hao Lu, Ying Ying Wang, Yuan Ping Feng, and Ze Xiang Shen. Uniaxial strain on graphene: Raman spectroscopy study and band-gap opening. *ACS nano*, 2(11):2301–2305, 2008.

[69] Andrea C Ferrari. Raman spectroscopy of graphene and graphite: disorder, electron–phonon coupling, doping and nonadiabatic effects. *Solid state communications*, 143(1-2):47–57, 2007.

[70] LM Malard, MAA Pimenta, G Dresselhaus, and MS Dresselhaus. Raman spectroscopy in graphene. *Physics reports*, 473(5-6):51–87, 2009.

[71] Andrea C Ferrari and Denis M Basko. Raman spectroscopy as a versatile tool for studying the properties of graphene. *Nature nanotechnology*, 8(4):235, 2013.

[72] Xu Du, Ivan Skachko, Anthony Barker, and Eva Y Andrei. Approaching ballistic transport in suspended graphene. *Nature nanotechnology*, 3(8):491–495, 2008.

[73] B Huard, N Stander, JA Sulpizio, and D Goldhaber-Gordon. Evidence of the role of contacts on the observed electron-hole asymmetry in graphene. *Physical Review B*, 78(12):121402, 2008.

[74] Salvador Barraza-Lopez, Mihajlo Vanević, Markus Kindermann, and Mei-Yin Chou. Effects of metallic contacts on electron transport through graphene. *Physical review letters*, 104(7):076807, 2010.

[75] Jonas D Buron, Filippo Pizzocchero, Peter U Jepsen, Dirch H Petersen, José M Caridad, Bjarke S Jessen, Timothy J Booth, and Peter Bøggild. Graphene mobility mapping. *Scientific reports*, 5:12305, 2015.

[76] Chul Lee, Joo Youn Kim, Sukang Bae, Keun Soo Kim, Byung Hee Hong, and EJ Choi. Optical response of large scale single layer graphene. *Applied Physics Letters*, 98(7):071905, 2011.

[77] VP Gusynin, SG Sharapov, and JP Carbotte. Unusual microwave response of dirac quasiparticles in graphene. *Physical review letters*, 96(25):256802, 2006.

[78] NMR Peres. Colloquium: The transport properties of graphene: An introduction. *Reviews of modern physics*, 82(3):2673, 2010.

[79] Fengnian Xia, Hugen Yan, and Phaedon Avouris. The interaction of light and graphene: basics, devices, and applications. *Proceedings of the IEEE*, 101(7):1717–1731, 2013.

[80] Jahan M Dawlaty, Shriram Shivaraman, Jared Strait, Paul George, Mvs Chandrashekhar, Farhan Rana, Michael G Spencer, Dmitry Veksler, and Yunqing Chen. Measurement of the optical absorption spectra of epitaxial graphene from terahertz to visible. *Applied Physics Letters*, 93(13):131905, 2008.

[81] EH Hwang, S Adam, and S Das Sarma. Carrier transport in two-dimensional graphene layers. *Physical review letters*, 98(18):186806, 2007.

[82] Kin Fai Mak, Matthew Y Sfeir, Yang Wu, Chun Hung Lui, James A Misewich, and Tony F Heinz. Measurement of the optical conductivity of graphene. *Physical review letters*, 101(19):196405, 2008.

[83] Kin Fai Mak, Long Ju, Feng Wang, and Tony F Heinz. Optical spectroscopy of graphene: From the far infrared to the ultraviolet. *Solid State Communications*, 152(15):1341–1349, 2012.

[84] Hugen Yan, Fengnian Xia, Wenjuan Zhu, Marcus Freitag, Christos Dimitrakopoulos, Ageeth A Bol, George Tulevski, and Phaedon Avouris. Infrared spectroscopy of wafer-scale graphene. *Acs Nano*, 5(12):9854–9860, 2011.

[85] Feng Wang, Yuanbo Zhang, Chuanshan Tian, Caglar Girit, Alex Zettl, Michael Crommie, and Y Ron Shen. Gate-variable optical transitions in graphene. *science*, 320(5873):206–209, 2008.

[86] ZQ Li, Eric A Henriksen, Z Jiang, Zhao Hao, Michael C Martin, P Kim, HL Stormer, and Dimitri N Basov. Dirac charge dynamics in graphene by infrared spectroscopy. *Nature Physics*, 4(7):532–535, 2008.

[87] Kentaro Nomura and Allan H MacDonald. Quantum transport of massless dirac fermions. *Physical review letters*, 98(7):076602, 2007.

[88] Jonas D Buron, David MA Mackenzie, Dirch H Petersen, Amaia Pesquera, Alba Centeno, Peter Bøggild, Amaia Zurutuza, and Peter U Jepsen. Terahertz wafer-scale mobility mapping of graphene on insulating substrates without a gate. *Optics express*, 23(24):30721–30729, 2015.

[89] Patrick R Whelan, Deping Huang, David Mackenzie, Sara A Messina, Zhancheng Li, Xin Li, Yunqing Li, Timothy J Booth, Peter U Jepsen, Haofei Shi, et al. Conductivity mapping of graphene on polymeric films by terahertz time-domain spectroscopy. *Optics Express*, 26(14):17748–17754, 2018.

[90] Lei Ren, Qi Zhang, Jun Yao, Zhengzong Sun, Ryosuke Kaneko, Zheng Yan, Sebastien Nanot, Zhong Jin, Iwao Kawayama, Masayoshi Tonouchi, et al. Terahertz and infrared spectroscopy of gated large-area graphene. *Nano Letters*, 12(7):3711–3715, 2012.

[91] Berardi Sensale-Rodriguez, Rusen Yan, Michelle M Kelly, Tian Fang, Kristof Tahy, Wan Sik Hwang, Debdeep Jena, Lei Liu, and Huili Grace Xing. Broadband graphene terahertz modulators enabled by intraband transitions. *Nature communications*, 3(1):1–7, 2012.

[92] Paul Drude. Zur elektronentheorie der metalle. *Annalen der physik*, 306(3):566–613, 1900.

[93] Neil W Ashcroft, N David Mermin, et al. Solid state physics [by] neil w. ashcroft [and] n. david mermin., 1976.

[94] John M Ziman. *Principles of the Theory of Solids*. Cambridge university press, 1972.

[95] Frederick Reif. *Fundamentals of statistical and thermal physics*. Waveland Press, 2009.

[96] Karsten Arts, René Vervuurt, Arkabrata Bhattacharya, Jaime Gómez Rivas, Johan Willem Oosterbeek, and Ageeth A Bol. Broadband optical response of graphene measured by terahertz time-domain spectroscopy and ftir spectroscopy. *Journal of Applied Physics*, 124(7):073105, 2018.

[97] LA Falkovsky. Optical properties of graphene. In *Journal of Physics: conference series*, volume 129, page 012004. IOP Publishing, 2008.

[98] Giriraj Jnawali, Yi Rao, Hugen Yan, and Tony F Heinz. Observation of a transient decrease in terahertz conductivity of single-layer graphene induced by ultrafast optical excitation. *Nano letters*, 13(2):524–530, 2013.

[99] Derek Abbott and Xi-Cheng Zhang. Special issue on t-ray imaging, sensing, and retection. *Proceedings of the IEEE*, 95(8):1509–1513, 2007.

[100] George Grüner and Claus Dahl. *Millimeter and submillimeter wave spectroscopy of solids*, volume 200. Springer, 1998.

[101] M Walther, P Plochocka, B Fischer, H Helm, and P Uhd Jepsen. Collective vibrational modes in biological molecules investigated by terahertz time-domain spectroscopy. *Biopolymers: Original Research on Biomolecules*, 67(4-5):310–313, 2002.

[102] Robert A Kaindl, Marc A Carnahan, D Hägele, R Lövenich, and Daniel S Chemla. Ultrafast terahertz probes of transient conducting and insulating phases in an electron–hole gas. *Nature*, 423(6941):734–738, 2003.

[103] M Schall, M Walther, and P Uhd Jepsen. Fundamental and second-order phonon processes in cdte and znte. *Physical Review B*, 64(9):094301, 2001.

[104] Charles A Schmuttenmaer. Exploring dynamics in the far-infrared with terahertz spectroscopy. *Chemical reviews*, 104(4):1759–1780, 2004.

[105] Donna Strickland and Gerard Mourou. Compression of amplified chirped optical pulses. *Optics communications*, 56(3):219–221, 1985.

[106] Ajay Nahata, David H Auston, Tony F Heinz, and Chengjiu Wu. Coherent detection of freely propagating terahertz radiation by electro-optic sampling. *Applied physics letters*, 68(2):150–152, 1996.

[107] Ajay Nahata, Aniruddha S Weling, and Tony F Heinz. A wideband coherent terahertz spectroscopy system using optical rectification and electro-optic sampling. *Applied physics letters*, 69(16):2321–2323, 1996.

[108] N Vieweg, N Krumbholz, T Hasek, R Wilk, V Bartels, C Keseberg, V Pethukhov, M Mikulics, L Wetenkamp, and M Koch. Fiber-coupled thz spectroscopy for monitoring polymeric compounding processes. In *Optical Measurement Systems for Industrial Inspection V*, volume 6616, page 66163M. International Society for Optics and Photonics, 2007.

[109] Tobias Kampfrath, Koichiro Tanaka, and Keith A Nelson. Resonant and nonresonant control over matter and light by intense terahertz transients. *Nature Photonics*, 7(9):680, 2013.

[110] Wai Lam Chan, Jason Deibel, and Daniel M Mittleman. Imaging with terahertz radiation. *Reports on progress in physics*, 70(8):1325, 2007.

[111] SS Dhillon, MS Vitiello, EH Linfield, AG Davies, Matthias C Hoffmann, John Booske, Claudio Paoloni, M Gensch, Peter Weightman, GP Williams, et al. The 2017 terahertz science and technology roadmap. *Journal of Physics D: Applied Physics*, 50(4):043001, 2017.

[112] Robert W Boyd. *Nonlinear optics*. Elsevier, 2003.

[113] Qi Wu and X-C Zhang. Free-space electro-optic sampling of terahertz beams. *Applied Physics Letters*, 67(24):3523–3525, 1995.

[114] Mark Fox. Optical properties of solids, 2002.

[115] Ronald Ulbricht, Euan Hendry, Jie Shan, Tony F Heinz, and Mischa Bonn. Carrier dynamics in semiconductors studied with time-resolved terahertz spectroscopy. *Reviews of Modern Physics*, 83(2):543, 2011.

[116] David J Griffiths. *Introduction to electrodynamics*. Prentice Hall New Jersey, 1962.

[117] RE Glover III and Ms Tinkham. Conductivity of superconducting films for photon energies between 0.3 and 4 0 k t c. *Physical Review*, 108(2):243, 1957.

[118] David G Cooke. *Time-resolved terahertz spectroscopy of bulk and nanoscale semiconductors*. 2007.

[119] Wei Cui, Aidan W Schiff-Kearn, Emily Zhang, Nicolas Couture, Francesco Tani, David Novoa, Philip St J Russell, and Jean-Michel Ménard. Broadband and tunable time-resolved thz system using argon-filled hollow-core photonic crystal fiber. *APL Photonics*, 3(11):111301, 2018.

[120] Hyunyong Choi, Ferenc Borondics, David A Siegel, Shuyun Y Zhou, Michael C Martin, Alessandra Lanzara, and Robert A Kaindl. Broadband electromagnetic response

and ultrafast dynamics of few-layer epitaxial graphene. *Applied Physics Letters*, 94(17):172102, 2009.

[121] Inhee Maeng, Seongchu Lim, Seung Jin Chae, Young Hee Lee, Hyunyong Choi, and Joo-Hiuk Son. Gate-controlled nonlinear conductivity of dirac fermion in graphene field-effect transistors measured by terahertz time-domain spectroscopy. *Nano letters*, 12(2):551–555, 2012.

[122] Jonas D Buron, Filippo Pizzocchero, Bjarke S Jessen, Timothy J Booth, Peter F Nielsen, Ole Hansen, Michael Hilke, Eric Whiteway, Peter U Jepsen, Peter Bøggild, et al. Electrically continuous graphene from single crystal copper verified by terahertz conductance spectroscopy and micro four-point probe. *Nano letters*, 14(11):6348–6355, 2014.

[123] Joo Youn Kim, Chul Lee, Sukang Bae, Keun Soo Kim, Byung Hee Hong, and EJ Choi. Far-infrared study of substrate-effect on large scale graphene. *Applied Physics Letters*, 98(20):201907, 2011.

[124] AJ Frenzel, CH Lui, W Fang, NL Nair, PK Herring, P Jarillo-Herrero, J Kong, and N Gedik. Observation of suppressed terahertz absorption in photoexcited graphene. *Applied Physics Letters*, 102(11):113111, 2013.

[125] Jean-Michel Guay, Ranjana Rautela, Samantha Scarfe, Petr Lazar, Saied Azimi, Cedric Grenapin, Alexei Halpin, Weixang Wang, Lukasz Andrzejewski, Ryan Plumadore, et al. Mechanistic insight into the limiting factors of graphene-based environmental sensors. *arXiv preprint arXiv:1911.05757*, 2019.

[126] Hassan A Hafez, X Chai, Y Sekine, M Takamura, K Oguri, I Al-Naib, MM Dignam, H Hibino, and T Ozaki. Effects of environmental conditions on the ultrafast car-

rier dynamics in graphene revealed by terahertz spectroscopy. *Physical Review B*, 95(16):165428, 2017.

[127] Callum J Docherty, Cheng-Te Lin, Hannah J Joyce, Robin J Nicholas, Laura M Herz, Lain-Jong Li, and Michael B Johnston. Extreme sensitivity of graphene photoconductivity to environmental gases. *Nature communications*, 3(1):1–6, 2012.

[128] Jichen Dong, Huan Wang, Hailin Peng, Zhongfan Liu, Kaili Zhang, and Feng Ding. Formation mechanism of overlapping grain boundaries in graphene chemical vapor deposition growth. *Chemical science*, 8(3):2209–2214, 2017.

[129] Tyler L Cocker, Devin Baillie, Miles Buruma, Lyubov V Titova, Richard D Sydora, Frank Marsiglio, and Frank A Hegmann. Microscopic origin of the drude-smith model. *Physical Review B*, 96(20):205439, 2017.

[130] Yung-Chang Lin, Chun-Chieh Lu, Chao-Huei Yeh, Chuanhong Jin, Kazu Suenaga, and Po-Wen Chiu. Graphene annealing: how clean can it be? *Nano letters*, 12(1):414–419, 2012.

[131] Haomin Wang, Yihong Wu, Chunxiao Cong, Jingzhi Shang, and Ting Yu. Hysteresis of electronic transport in graphene transistors. *ACS nano*, 4(12):7221–7228, 2010.

[132] A Piazza, F Giannazzo, G Buscarino, G Fisichella, A La Magna, F Roccaforte, M Cannas, FM Gelardi, and S Agnello. Graphene p-type doping and stability by thermal treatments in molecular oxygen controlled atmosphere. *The Journal of Physical Chemistry C*, 119(39):22718–22723, 2015.

[133] Shaffique Adam, EH Hwang, VM Galitski, and S Das Sarma. A self-consistent theory for graphene transport. *Proceedings of the National Academy of Sciences*, 104(47):18392–18397, 2007.

[134] Jens Martin, N Akerman, G Ulbricht, T Lohmann, JH v Smet, K Von Klitzing, and Amir Yacoby. Observation of electron–hole puddles in graphene using a scanning single-electron transistor. *Nature physics*, 4(2):144–148, 2008.

[135] AV Shytov, MI Katsnelson, and LS Levitov. Atomic collapse and quasi–rydberg states in graphene. *Physical Review Letters*, 99(24):246802, 2007.

[136] Yang Wang, Dillon Wong, Andrey V Shytov, Victor W Brar, Sangkook Choi, Qiong Wu, Hsin-Zon Tsai, William Regan, Alex Zettl, Roland K Kawakami, et al. Observing atomic collapse resonances in artificial nuclei on graphene. *Science*, 340(6133):734–737, 2013.

[137] Matthew J Hollander, Michael LaBella, Zachary R Hughes, Michael Zhu, Kathleen A Trumbull, Randal Cavalero, David W Snyder, Xiaojun Wang, Euichul Hwang, Suman Datta, et al. Enhanced transport and transistor performance with oxide seeded high-κ gate dielectrics on wafer-scale epitaxial graphene. *Nano letters*, 11(9):3601–3607, 2011.

[138] LA Ponomarenko, R Yang, TM Mohiuddin, MI Katsnelson, KS Novoselov, SV Morozov, AA Zhukov, F Schedin, EW Hill, and AK Geim. Effect of a high-κ environment on charge carrier mobility in graphene. *Physical review letters*, 102(20):206603, 2009.

[139] Fang Chen, Jilin Xia, David K Ferry, and Nongjian Tao. Dielectric screening enhanced performance in graphene fet. *Nano letters*, 9(7):2571–2574, 2009.

[140] TO Wehling, KS Novoselov, SV Morozov, EE Vdovin, MI Katsnelson, AK Geim, and AI Lichtenstein. Molecular doping of graphene. *Nano letters*, 8(1):173–177, 2008.

[141] MI Katsnelson and AK Geim. Electron scattering on microscopic corrugations in graphene. *Philosophical Transactions of the Royal Society A: Mathematical, Physical and Engineering Sciences*, 366(1863):195–204, 2008.

[142] Aniruddha Konar, Tian Fang, and Debdeep Jena. Effect of high-κ gate dielectrics on charge transport in graphene-based field effect transistors. *Physical Review B*, 82(11):115452, 2010.